

Publication 01/02

A validation of parallel multiblock CFD against the GAMM Francis water turbine runner at best efficiency and off-design operating conditions

Håkan Nilsson and Lars Davidson

Department of Thermo and Fluid Dynamics
CHALMERS UNIVERSITY OF TECHNOLOGY
Göteborg, Sweden, August 2001

A validation of parallel multiblock CFD against the GAMM Francis water turbine runner at best efficiency and off-design operating conditions

H. Nilsson and L. Davidson

Abstract

The CALC-PMB (Parallel MultiBlock) CFD code is used to predict the flow in the GAMM Francis water turbine runner at best efficiency and off-design operating conditions. The computations are made in a rotating coordinate system, where the computational domain starts at the guide vanes and ends at the entrance to the draft tube. Because the guide vanes are not included in the computations, the inlet boundary conditions are obtained from an extrapolation of measurements before the runner. The flow is assumed to be steady and periodic. This allows periodic computations of a single runner blade, which considerably reduces the size of the computational domain. Most hydraulic turbine computations found in the literature use the wall function approach to further reduce the size of the computational domain. However, the wall function approach is based on local equilibrium assumptions in fully developed boundary layers, which is not found in turbine runners. To bring the computations one step further, this work uses a low Reynolds number turbulence model that can be used all the way to the wall. The computational results that are compared to measurements are the circumferentially averaged velocity and static pressure distributions, the runner blade static pressure distributions, the torque and the efficiency. The comparisons show that most of the flow features observed are captured by the computations. For the flow features that are not captured properly, the assumption of steady and periodic flow is not applicable. This work argues that steady periodic multiblock CFD can be used for water turbine runner computations, but that transient computations of the complete runner are required to capture all the flow features.

Keywords: CFD, Finite volume, Numerical, Turbulence, Parallel, Multiblock, Francis, Turbine, Turbomachinery, Validation.

Contents

Abstract	i
Acknowledgements	v
Nomenclature	vii
Acronyms	ix
1 Introduction	1
2 Numerical method	3
2.1 Turbulence model	3
2.2 Equations	4
2.3 Boundary conditions	5
2.3.1 Static pressure	5
2.3.2 Walls	5
2.3.3 Inlet	6
2.3.4 Outlet	7
2.3.5 Periodic boundaries	7
2.3.6 Degenerate boundaries	8
2.4 Numerical considerations	8
3 Description of the GAMM Francis turbine	9
3.1 Geometrical information	9
3.1.1 Remarks on the geometrical information	9
3.1.2 Computational grid	9
3.2 Measurements	10
3.2.1 Best efficiency operating condition	10
3.2.2 Off-design operating conditions	11
3.2.3 Remarks on the measurements	13
4 Validation of the computational results	15
4.1 Experimental validation of the computational results	15
4.1.1 Specific energy, torque and efficiency	15
4.1.2 Circumferentially averaged flow survey	16
4.1.3 Runner blade static pressure distribution	23
4.2 Numerical validation of the computational results	23
4.2.1 Convergence	30
4.2.2 Low Reynolds wall treatment	31
5 Flow feature visualization	33
5.1 Streamlines	33
5.2 Surface static pressure distribution	33
5.3 Static pressure iso-surfaces	33
6 Conclusion	39
References	41

Acknowledgements

This work was financed and supported by ELFORSK (Swedish Electrical Utilities Research and Development Company), the Swedish National Energy Administration and GE Energy (Sweden) AB.

Part of the work was carried out during the first author's three-month visit at EPFL in the fall of 1999.

Computer time at UNICC, Chalmers, is gratefully acknowledged.

Nomenclature

The normalization factors are the same as those used in the GAMM proceedings [1] and the IMHEF [7] computations.

$C_m = \frac{c_m}{\sqrt{2E}} = \sqrt{C_r^2 + C_z^2}$	Absolute meridional velocity coefficient [–]
$C_p = \frac{P - P_{ref}}{\rho E}$	Static pressure coefficient [–]
$C_r = \frac{c_r}{\sqrt{2E}}$	Absolute radial velocity coefficient [–]
$C_u = \frac{c_u}{\sqrt{2E}}$	Absolute tangential velocity coefficient [–]
$C_z = \frac{c_z}{\sqrt{2E}}$	Absolute axial velocity coefficient [–]
C_v ($v = m/r/u/z$)	General velocity coefficient [–]
E	Specific hydraulic energy [J/kg]
P	Static pressure [N/m^2]
P^*	Reduced static pressure [N/m^2]
P_{ref}	Reference static pressure [N/m^2]
Q	Volume flow [m^3/s]
$R_{ref} = 0.2m$	Reference radius [m]
T	Runner torque [Nm]
U_i	Mean relative Cartesian velocity vector [m/s]
c_m	Absolute meridional velocity [m/s]
c_r	Absolute radial velocity [m/s]
c_u	Absolute tangential velocity [m/s]
c_z	Absolute axial velocity [m/s]
c_v ($v = m/r/u/z$)	General velocity component [m/s]
g_i	Gravitational acceleration vector [m/s^2]
k	Turbulent kinetic energy [m^2/s^2]
p'	Pressure correction [N/m^2]
s	Normalized abscissa [–]
$t^* = \frac{T}{\rho \pi E R_{ref}^3}$	Normalized torque [–]
x_i	Cartesian position vector [m]
$\alpha = \arctan\left(\frac{C_m}{C_u}\right)$	Absolute flow angle [–]
$\beta = \arctan\left(\frac{C_m}{\Omega R / \sqrt{2E} - C_u}\right)$	Relative flow angle [–]
ε	Dissipation rate [m^2/s^3]
ϵ_{ijk}	Levi-Cevita's permutation function [–]
$\eta = \frac{T\Omega}{\rho Q E}$	Efficiency [–]
μ	Dynamic viscosity [Ns/m^2]
μ_t	Turbulent dynamic viscosity [Ns/m^2]
ν	Kinematic viscosity [m^2/s]
ν_t	Turbulent kinematic viscosity [m^2/s]
Ω	Angular rotation [s^{-1}]
Ω_i	Angular rotation vector [s^{-1}]
ω	Specific dissipation rate [s^{-1}]
$\varphi = \frac{Q}{\pi \Omega R^3}$	Volume flow coefficient [–]

$$\psi = \frac{2E}{\Omega^2 R^2}$$

$$\rho$$

Energy coefficient $[-]$
Density (of water) $[kg/m^3]$

For reasons of poor draft tube behaviour, the measured specific hydraulic energy, E , was determined both according to the IEC standard¹

$$E = \frac{P_I}{\rho} + \frac{Q_I^2}{2A_I^2} + gZ_I - \frac{P_{\bar{I}}}{\rho} - \frac{Q_{\bar{I}}^2}{2A_{\bar{I}}^2} - gZ_{\bar{I}}$$

and using a reference section in the cone

$$E = \frac{P_I}{\rho} + \frac{Q_I^2}{2A_I^2} + gZ_I - \frac{P_{ref}}{\rho} - \frac{Q_{ref}^2}{2A_{ref}^2} - gZ_{ref}$$

where the standard section (I) is taken at the machine inlet, the standard reference section (\bar{I}) is placed at the outlet of the draft tube and A is the area of the reference sections. Because the machine inlet is not included in the computations, the computed specific hydraulic energy is determined by integration at the inlet and outlet of the computational domain. The computed values are compared with the measured specific hydraulic energy using the cone reference section.

The computed runner torque, T , is determined by integration of the axial component of the moment acting on the runner blades.

¹Hydraulic turbines, storage pumps and pump-turbines - Model acceptance tests. <http://www.iec.ch/>

Acronyms

BFC	Boundary Fitted Coordinates (a version of CALC)
CALC	Name of an in-house CFD code
CFD	Computational Fluid Dynamics
EPFL	École Polytechnique Fédérale de Lausanne
ERCOFTAC	European Research Community On Flow Turbulence And Combustion
GAMM	Gesellschaft für Angewandte Mathematik und Mechanik
GE	General Electrics
IEC	International Electrotechnical Commission
IMH	Institut de Machines Hydrauliques
IMHEF	Institut de Machines Hydrauliques et de Mécanique des Fluides
MPI	Message Passing Interface
NOW	Network Of Workstations
PMB	Parallel MultiBlock (a version of CALC)
PVM	Parallel Virtual Machine
SIMPLEC	Semi-Implicit Method for Pressure-Linked Equations, Consistent
SPMD	Single Program Multiple Data
UNICC	Unix Numeric Intensive Calculations at Chalmers

1 Introduction

This work was initiated by a need for validation of the CALC-PMB [5, 11–13] CFD code for hydraulic turbine applications. The code has been developed and used for computations of the turbulent flow in a Kaplan runner since 1997. It was validated against academic flow cases but not for applications as complicated as hydraulic turbines. During the development of the code, pure intuition of what the flow should look like and the fact that the computations converged served as an indication that the code produced good results. Intuition about hydraulic turbines was at least initially a product of the thinking of the turbine manufacturer, GE Energy (Sweden) AB, at that time called Kvaerner Turbin AB. Intuition about general fluid dynamics, numerical experience and, in the later stages, intuition about hydraulic turbines were gained from the CFD code developer at Chalmers. However, as the results became more and more trustworthy, a need arose for more sophisticated validation. For the above-mentioned Kaplan turbine, the only available measurements are the rotational speed, volume flow, head and torque. This can of course be used to achieve some degree of validation, but it is desirable to gain a more detailed picture of the behaviour of the turbine.

In 1999, contact was set up with the IMH-IMHEF-EPFL water turbine laboratory in Lausanne, Switzerland, which has publically available measurements of a complete hydraulic Francis turbine model. These measurements were made in 1989 for the *GAMM Workshop on 3D-Computation of Incompressible Internal Flows* [17] in Lausanne. The GAMM Francis runner is also used in the annual *ERCOFTAC Seminar and Workshop on Turbomachinery Flow Predictions*². An international collaboration was established, where the CALC-PMB CFD code was validated against the GAMM Francis runner. Part of the work was done at IMH-IMHEF-EPFL, where the first author spent three months in the fall of 1999, and part at the Department of Thermo and Fluid Dynamics at Chalmers.

This work computes the turbulent flow in the GAMM Francis runner at the best efficiency operating point and at four off-design operating points. The computational domain starts at the guide vanes, where inlet boundary conditions derived from an extrapolation of the measurements before the runner blades are applied. The guide vanes are not included in the present work. The inlet boundary conditions are axi-symmetric and the computations are periodic.

Computations similar to those presented here have been made at IMHEF [7], where computational results of the GAMM runner using two different commercial CFD codes, TASCflow and N3S, were compared with measurements. A coupled computation of the best efficiency operating point including stay vanes, guide vanes and runner was also made. No significant differences were however observed between the single and coupled computations. The IMHEF computations were done on a coarse mesh (less than 100,000 nodes) using the standard $k - \varepsilon$ turbulence model with wall functions. The reason for this was, according to the authors, to keep the computing time reasonable for industrial use.

To bring the computations one step further and to be able to resolve clearance flow (hub and tip clearance flow in Kaplan turbines and guide vane clearance flow), this work uses a low Reynolds number turbulence model that can be used all the way to the wall. The model may be modified to include effects of, for instance, wall surface roughness. This has not been done in the present work but could be done in the future if it is found that the modifications would affect the flow features. There is no detailed investigation of the influence of the turbulence model on the flow in this work.

²<http://imhefwww.epfl.ch/ERCOFTAC/>

2 Numerical method

This section gives a brief description of the CALC-PMB [5, 11–13] CFD code. The interested reader is referred to the references for a thorough description.

A single structured block sequential finite volume CFD solver, CALC-BFC [5], was extended with message passing utilities for parallel computations of turbulent flow in complex multiblock domains [11, 13]. The main features of the resulting SPMD code, CALC-PMB, are the use of conformal block structured boundary fitted coordinates, a pressure correction scheme (SIMPLEC [6]), Cartesian velocity components as the principal unknowns, and collocated grid arrangement together with Rhie and Chow interpolation. Rotational terms that arise from rotation of the computational domain (Coriolis and centrifugal force) are included in the momentum equations. A second order upwind Van-Leer scheme is used in discretizing the equations. The parallel multiblock algorithm uses two ghost cell planes at the block interfaces. The message passing at the interfaces is hidden behind a high level parallel multiblock library with data structures that fit CALC-PMB, and the underlying message passing interface (PVM or MPI) is chosen at compilation time. The calls for parallel multiblock routines in the code are thus completely independent of the message passing interface that is used. Thus most of the parallelism is hidden from the user, who can easily manipulate the code for his/her purposes using the high level parallel multiblock library, if necessary. The advanced user may easily add optional message passing interfaces if needed.

The code may be run on everything from inhomogeneous NOW to Beowulf Linux clusters and distributed and shared memory supercomputers. It can read a predefined multiblock topology with connectivity information from the disk or subdivide single block domains into sub-blocks of equal size for load balanced parallel computation. The gains of this operation are several: the computational speed may be increased, larger problems may be solved since the memory requirement is divided between the processors (when using distributed machines), more exact solutions may be obtained because of the extra memory available and parallel supercomputers may be employed.

The parallel efficiency of the code is excellent for large 3D load balanced applications. However, load balancing is difficult for complicated geometries such as hydraulic turbines, especially when computing Kaplan runners with tip clearance, where the block sizes may differ by an order of magnitude.

2.1 Turbulence model

The two equation low Reynolds number $k-\omega$ turbulence model of Wilcox [18] is used to resolve the turbulent flow in runner hub and tip clearances (Kaplan turbines), guide vane clearances and in the boundary layers. This is a simple turbulence model that enhances computational stability. With no viscous damping in the model's closure coefficients and without the aid of wall functions, the model equations can be solved through the viscous sub-layer, down to the wall.

The main advantage of this model in hydraulic turbine applications is its ability to resolve the boundary layer without complicated correction functions on the basis of distance to the wall. Surface boundary conditions that account for flow over rough surfaces or other flow features are available. However, this work treats all surfaces as smooth. No effect of rotation is included in the k and ω equations. Higher order turbulence models that take into account rotational effects, streamline curvature effects and adverse pressure gradients effects etc. may be examined in the future. However, until greater experience is gained of CFD in water turbines, simple turbulence

models may as well be used. Detailed investigations of the influence of the turbulence model on the computed flow is beyond the scope of this work.

Most computations of the turbulent flow in hydraulic turbines found in the literature use wall functions instead of resolving the boundary layers with a low Reynolds number model because low Reynolds number models are very time consuming as a result of the large number of nodes and the slower convergence of a finer resolution. However, the wall function approach is based on local equilibrium assumptions in fully developed boundary layers. Neither of these assumptions are true in a hydraulic turbine. Yet the wall function approach performs surprisingly well. However, with increasing computer power and refined numerical solution schemes, future industrial computations will most likely use turbulence models that resolve the turbulent boundary layers. The main aim in the development of CALC-PMB for hydraulic turbines is to study the tip clearance effects in Kaplan turbines, where a low Reynolds number model is the most appropriate choice.

2.2 Equations

The equations used for the computations are briefly described below.

The stationary Reynolds time-averaged continuity and Navier Stokes equations for incompressible flow in a rotating frame of reference read [4, 9]

$$\frac{\partial \rho U_i}{\partial x_i} = 0$$

$$\frac{\partial \rho U_i U_j}{\partial x_j} = -\frac{\partial P}{\partial x_i} + \frac{\partial}{\partial x_j} \left((\mu + \mu_t) \frac{\partial U_i}{\partial x_j} \right) + \rho g_i - \rho \epsilon_{ijk} \epsilon_{klm} \Omega_j \Omega_l x_m - 2\rho \epsilon_{ijk} \Omega_j U_k$$

where $-\epsilon_{ijk} \epsilon_{klm} \Omega_j \Omega_l x_m$ is the centripetal term and $-2\epsilon_{ijk} \Omega_j U_k$ is the Coriolis term, owing to the rotating coordinate system. Because of the potential nature of the pressure, gravitational and centripetal terms [9], they are put together during the computations, in what is often referred to as a *reduced* pressure gradient

$$-\frac{\partial P^*}{\partial x_i} = -\frac{\partial P}{\partial x_i} + \rho g_i - \rho \epsilon_{ijk} \epsilon_{klm} \Omega_j \Omega_l x_m$$

Thus, a relation for the *reduced* pressure is

$$P^* = P - \rho g_i x_i + \rho \epsilon_{ijk} \epsilon_{klm} \Omega_j \Omega_l x_m x_i$$

When post-processing, the variation of the gravity term is assumed to be negligible and the centripetal term is simply subtracted from the *reduced* pressure.

The $k - \omega$ model of Wilcox [18] for the turbulent kinetic energy, k , and the specific dissipation rate, ω , reads

$$\begin{aligned} \frac{\partial \rho U_j k}{\partial x_j} &= \frac{\partial}{\partial x_j} \left[\left(\mu + \frac{\mu_t}{\sigma_k} \right) \frac{\partial k}{\partial x_j} \right] + P_k - \rho \beta^* \omega k \\ \frac{\partial \rho U_j \omega}{\partial x_j} &= \frac{\partial}{\partial x_j} \left[\left(\mu + \frac{\mu_t}{\sigma_\omega} \right) \frac{\partial \omega}{\partial x_j} \right] + \frac{\omega}{k} (c_{\omega 1} P_k - c_{\omega 2} \rho k \omega) \end{aligned}$$

where the turbulent viscosity, μ_t , is defined as

$$\mu_t = \rho \frac{k}{\omega}$$

The production term reads

$$P_k = \mu_t \left(\frac{\partial U_i}{\partial x_j} + \frac{\partial U_j}{\partial x_i} \right) \frac{\partial U_i}{\partial x_j}$$

and the closure coefficients are defined from experiments as

$$\beta^* = 0.09, c_{\omega 1} = \frac{5}{9}, c_{\omega 2} = \frac{3}{40}, \sigma_k = 2 \text{ and } \sigma_\omega = 2$$

2.3 Boundary conditions

Boundary conditions for the static pressure, the velocity components and the turbulent quantities are described in the following sections. The same boundary condition is used for the static pressure at all boundaries, while all the other variables have different boundary conditions at different kinds of boundaries.

2.3.1 Static pressure

The static pressure is extrapolated at all boundaries according to

$$\frac{\partial^2 P}{\partial n^2} = 0$$

where n is the coordinate direction normal to the boundary. In this way, the pressure is not fixed to any level. Instead, a reference point is chosen at which the pressure is set to zero.

The pressure correction, p' , of the SIMPLEC method has an implicit homogeneous Neumann boundary condition on all boundaries [16], i.e.

$$\frac{\partial p'}{\partial n} = 0$$

where n is the coordinate direction normal to the boundary.

2.3.2 Walls

Boundary conditions for the k and ω equations of the $k - \omega$ turbulence model are

$$\begin{aligned} k &= 0 \\ \omega &= \frac{6\nu}{c_{\omega 2} y^2} \end{aligned} \tag{2.1}$$

where $c_{\omega 2} = 3/40$ and y is the wall-normal distance. The ω boundary condition is applied at the node closest to the wall, in the viscous sub-layer at $y^+ \approx 2.5$.

The velocity components are set to zero (no-slip) on walls that are stationary relative to the computational domain. If the walls are rotating relative to the computational domain, the relative rigid body velocity at the wall is simply set as a Dirichlet condition.

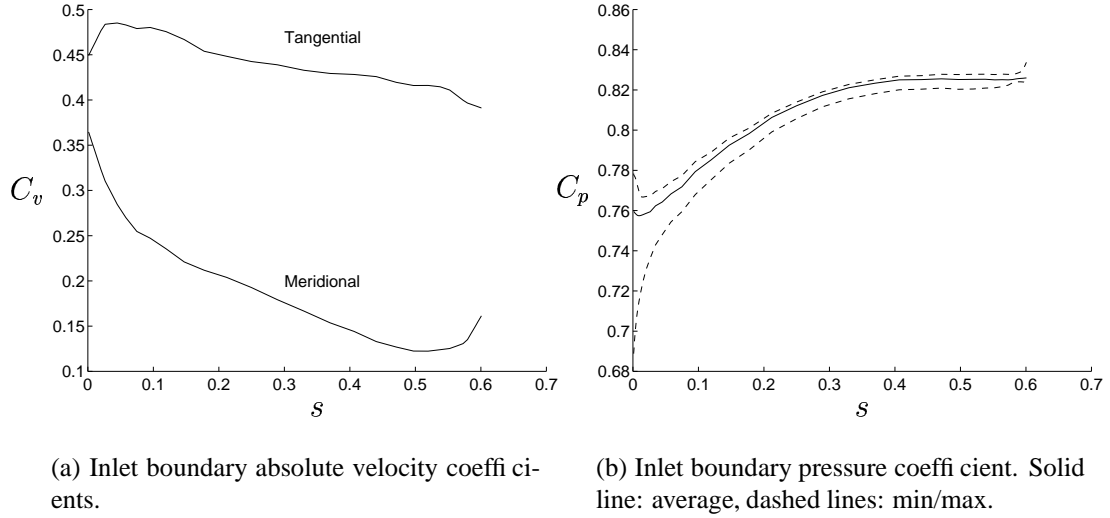


Figure 2.1: Inlet boundary condition, operating point 1.

2.3.3 Inlet

At an inlet, all flow properties except the static pressure are prescribed. They can be interpolated from experimental data or taken from a fully developed profile, such as a parabolic profile for laminar flow or a 1/7th profile for a turbulent flow. For the GAMM computations, the runner inlet boundary conditions for the velocity profiles are derived from a potential flow extrapolation, to $R = 239\text{mm}$ (see figure 3.1, section 3.1.1), of the measurements upstream from the runner. This extrapolation assumes that the angular momentum and the mass flow are conserved between the measured values and the extrapolated values. The reason for choosing this extrapolation technique is that it was used by Gros *et al.* [7] and its use here allows comparisons of the computations. The resulting inlet velocity boundary condition for the tangential and radial velocity components for the best efficiency operating point is shown in figure 2.1(a). The normalized abscissa, s , is defined as the distance from the lower ring along the measurement axis, normalized by the reference radius, R_{ref} . The axial velocity coefficient is set to zero. These boundary conditions are very similar to what was obtained from the separate guide vane computations by Nilsson and Davidson [14] that were used as inlet boundary conditions for Kaplan runner computations. The runner inlet static pressure distribution given by the computations for the best efficiency operating point is shown in figure 2.1(b). The continuous line is the circumferentially averaged static pressure and the dashed lines are the minimum and maximum values along the circumference. The inlet static pressure is thus periodic but not axisymmetric. The largest non-axi-symmetry is close to the shroud, which corresponds to the region closest to the leading edge of the runner blades. It could be argued that this non-axi-symmetry should make the velocity profiles at the inlet non-axisymmetric as well or that the inlet should be extrapolated even further away from the leading edges of the runner blades. However, the flow is highly accelerated at the extrapolated inlet and there are guide vanes in this region, which makes axis-symmetry only a more or less good assumption. Coupled transient computations could be made to study this effect, but that is beyond the scope of this work. Preliminary calculations with a coarse grid and axi-symmetric inlet boundary conditions even closer to the leading edge of the runner blades have been made and achieved surprisingly good results. The extrapolation used in this work is therefore considered sufficient.

The runner inlet boundary conditions for the turbulent quantities are difficult to prescribe. With non-coupled axi-symmetric boundary conditions, the state of the art is to assume a turbulent intensity and a turbulent length scale and to apply constant turbulent properties at the inlet. The definition of the turbulent intensity used in this work is the same as is used in the TASCflow CFD code. The inlet turbulent kinetic energy is prescribed as

$$k_{in} = \frac{3}{2} \gamma^2 \overline{C_{in}}^2$$

where γ is the turbulent intensity and $\overline{C_{in}}^2$ is the inlet average absolute velocity squared. The turbulent length scale is used together with dimensional analysis to set the inlet boundary condition for ω , in the case of the Wilcox model as

$$\omega_{in} = \frac{k_{in}^{1/2}}{\beta^* l}$$

where $\beta^* = 0.09$ and l is the turbulent length scale. For the computations made in this work, a turbulent intensity of 5% and a turbulent length scale of 1/3 of the inlet channel height are assumed. These numbers are somewhat arbitrary but it is not expected that their exact values are influential, since the source terms of the k and ω equations will be much larger than the history effects as soon as the flow reaches the runner. According to the ERCOFTAC description, the turbulent intensity was estimated to 3%. How this value has been obtained is however not specified.

2.3.4 Outlet

At a large outlet, sufficiently far downstream and without area change, the flow may be assumed to be fully developed, which implies negligible streamwise gradients of all variables, i.e.

$$\frac{\partial \Phi}{\partial n} = 0$$

where n is the coordinate direction normal to the outlet.

In order to get a mathematically well posed SIMPLEC algorithm, mass flux must be globally conserved [2]. This is a constraint necessary for the pressure correction equation to be consistent. It also increases the convergence rate considerably and has positive effects on open boundaries where there is inflow. A velocity increment is computed as

$$u_{incr} = \frac{\dot{m}_{in} - \dot{m}_{out}^{comp}}{\rho A_{out}}$$

where \dot{m}_{in} is the convection into the domain at the inlet, \dot{m}_{out}^{comp} is the computed convection out of the domain at the outlet (computed from $\partial c_v / \partial n = 0$) and A_{out} is the outlet area. The velocity increment is added to the computed velocity at the outlet, i.e.

$$u_{out} = u_{out}^{comp} + u_{incr}$$

This ensures that global continuity is fulfilled at each iteration.

2.3.5 Periodic boundaries

A rotational transformation of the velocity vectors [11], about the axis of rotation, is applied at rotational periodic boundaries. The periodic boundaries may then be treated as though they were connected to each other, since rotational periodicity has no impact on scalar quantities.

2.3.6 Degenerate boundaries

A cylindrical degenerate boundary is the boundary obtained when two of the boundary edges in a structured block are merged, forming a line boundary. At the degenerate boundary along the rotational axis, under the GAMM Francis turbine hub, the tangential velocity is set to zero and all other variables have a homogeneous Neumann boundary condition [11].

2.4 Numerical considerations

All the geometry between the inlet of the stay vanes and the outlet of the draft tube, as well as measurements at several locations are available for the GAMM Francis turbine. Only the 13-blade Francis runner is computed in this work. If the spiral casing distributes the flow axisymmetrically (a good assumption according to measurements), it is reasonable to believe that a rotationally stationary representation of the runner flow is periodic over an angle of $360/13$ degrees. This kind of periodic flow assumption is state of the art in water turbine CFD and is required in order to obtain a steady solution. Together with the periodic boundary conditions described in section 2.3.5, this assumption reduces the computational domain to $1/13$ th of its original size. Thus, only one runner blade passage has to be computed.

Rotational effects are included in the momentum equations [11] since the computational domain is rotating. At this stage, the $k - \omega$ model of Wilcox [18] is used without terms for rotational effects. This is common in turbomachinery computations for reasons of numerical stability and the small importance of such terms in these kinds of industrial applications [10].

To remove many of the boundary condition assumptions, complete turbine simulations (including spiral casing, distributor, runner and draft tube) are commonly done. The drawbacks of these simulations are that they usually use wall functions and that they still apply the above-mentioned assumptions, such as axisymmetric runner inlet conditions and periodicity. These computations tend to become very large and CPU demanding, and sufficiently fine grids to give accurate solutions can usually not be afforded. Also, additional features of the computational code, such as sliding grid interfaces, must be implemented. A sufficiently resolved transient complete turbine simulation without periodic and axis-symmetric assumptions and with a good interface between the rotating and stationary parts would be required to study transient effects in detail. This cannot be done with the present computational power.

3 Description of the GAMM Francis turbine

The test model corresponds to a Francis turbine of medium/high specific speed. It was designed at IMHEF for experimental research study in the hydraulic laboratory. The model was used as a test case in the 1989 GAMM workshop, where all the geometrical information, including stay vanes, guide vanes, runner and draft tube, and the best efficiency measurements were available. Of course, several off-design condition measurements have been made at IMHEF for internal use. Some of these measurements, namely the best efficiency operating point and four off-design operating conditions, are used in this work. The runner is also used as a test case in the annual ERCOFTAC Seminar and Workshop on Turbomachinery Flow Predictions.

3.1 Geometrical information

The spiral casing of the GAMM turbine was designed to give a constant meridional velocity distribution, and fillets were added on both sides of the distributor inlet in order to achieve well-defined inlet conditions. The distributor consists of 24 stay vanes and 24 guide vanes. The runner has 13 blades and its external diameter is $0.4m$, so the reference radius is $R_{ref} = 0.2m$. The draft tube is simple, without any inner pillar.

Detailed geometry files were available for the GAMM workshop. The geometry was defined as profiles of the meridional contour (figure 3.1), the two-dimensional profiles of the stay vanes and guide vanes and 17 profiles of the runner blades. There was also a detailed description of the draft tube. Detailed geometry files for the runner are available for the ERCOFTAC workshop.

3.1.1 Remarks on the geometrical information

The geometric information from a combination of the available GAMM and ERCOFTAC descriptions is used, since a few discrepancies were found between the descriptions. It should first be noted that the geometrical descriptions of the runner are very similar except for the following discrepancies.

The meridional contour of the model differs between the descriptions, see figure 3.1. The ERCOFTAC hub has been extended to asymptotically approach the rotational axis, while the GAMM hub is cut at $-76.2mm$. The GAMM distributor ring extends to radius $R = 346mm$, but the ERCOFTAC definition extends this to radius $R = 450mm$. The radius of the runner band at the lower end of the band (close to the middle axis shroud point) is too large in the ERCOFTAC definition, since it does not fit with any other geometrical information (figure 3.1(b)). The runner outlet of the ERCOFTAC definition is much closer to the runner and includes neither the reference point nor the measured outlet axis. In the ERCOFTAC measurement files, the length of the outlet measurement axis is $219.1mm$, which is $0.72mm$ more than is possible according to the geometry definition. The GAMM runner description has a sharp trailing edge while the ERCOFTAC runner description has a blunt trailing edge.

The ERCOFTAC runner blade description (with a blunt trailing edge) is used for the computations in this work. The diffuser after the runner band is described by the measurement points and the axisymmetric parts of the GAMM draft tube, according to figure 3.1. The rest of the meridional contour of the runner is taken from the GAMM description.

3.1.2 Computational grid

The selected geometrical descriptions of the GAMM Francis runner, together with the low Reynolds number turbulence model requirements, resulted in a multiblock computational grid

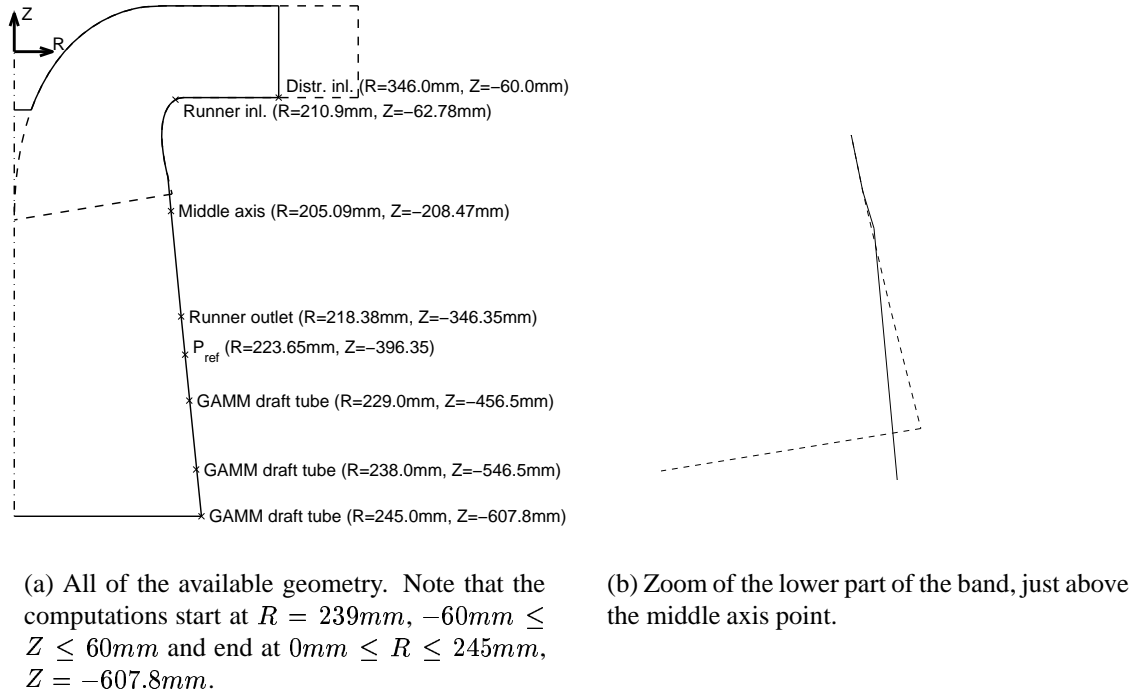


Figure 3.1: The meridional contour of the GAMM/ERCOFTAC Francis turbine. The axis of rotation is dash-dotted, the GAMM contour has solid lines and the ERCOFTAC contour has dashed lines. The marked points are from the GAMM description.

with five structured blocks and 560 736 control volumes. The grid surfaces that are attached to the hub and the runner blades are shown in figure 3.2.

3.2 Measurements

The measurements of the best efficiency operating condition and four off-design operating conditions are used in this work.

3.2.1 Best efficiency operating condition

For the GAMM workshop, detailed measurements for the best efficiency operating point ($\varphi = 0.286$, $\psi = 1.07$, $\eta = 0.92$) were available. The database comprised integral properties of the flow, such as torque ($t^* = 0.25577$) and global volume flow rate ($Q = 0.372m^3/s$), detailed pressure and velocity distribution measurements on some specified (non moving) axes and pressure distribution measurements on the blades of the runner in motion.

The pressure and velocity distribution measurements were made at the inlet of the distributor, at the inlet of the runner, just after the runner blades, at the inlet of the draft tube and at the outlet of the draft tube. The measurements were done using a 6mm diameter five-hole pressure probe, which gives the three components of the local flow components and the local static pressure. The flow behaviour at the outlet of the draft tube did not allow for detailed measurements with the available instrumentation, however, because of flow instabilities.

The runner measurement axes are shown in figure 3.3 and are defined as follows. The measured inlet axis is oblique, making an angle of 20 degrees with the vertical, and intersects

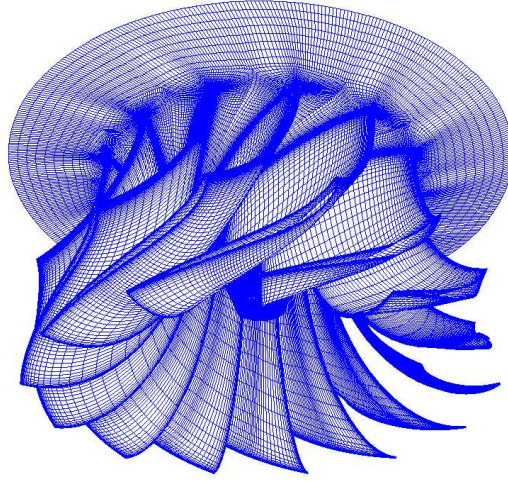


Figure 3.2: The Francis turbine runner multiblock grid used in this work. Note that all 13 blade passages are shown, although the simulations are carried out in one blade passage employing periodic boundary conditions.

the shroud at $R = 210.9mm$ and $Z = -62.78mm$. The measured middle axis is oblique and located just under the trailing edges of the blades. It makes an angle of 55 degrees with the vertical and intersects the shroud at $R = 205.09mm$ and $Z = -208.47mm$. The measured outlet axis is horizontal and intersects the shroud at $R = 218.38mm$ and $Z = -346.35mm$. Note that the inlet axis is not used as the inlet boundary in the computations, see section 2.3.3.

Pressure transducers provided the static pressure distribution on the runner blades along three profiles of the blades (figure 3.4). As the pressure transducer assembling process allowed placing three transducers on each blade, the measurements were made on several blades.

A reference static pressure was measured at the reference point (index *ref*), on the shroud at $R = 223.65mm$ and $Z = -396.35mm$ (figure 3.3).

The specific energy, E , was measured between the inlet section of the turbine and the reference section (index *ref*) in the diffuser.

The accuracy of the test instrumentation was claimed to be far better than the IEC model turbine acceptance test code requirements [1].

3.2.2 Off-design operating conditions

In conjunction with the best efficiency measurements made for the GAMM workshop, some off-design measurements were done. These measurements were not available at the workshop but were used in work by Gros *et al.* [7] in comparing the computational results of the TASCflow and N3S commercial CFD codes with measurements. The measurements, similar to those of the best efficiency operating point, for four off-design operating conditions are used in this work. The operating conditions studied are summarized in table 3.1 and figure 3.5. The best efficiency in the table is taken from the measurement report [1], which agrees with is seen in figure 3.5. The off-design efficiencies in the table are visually extracted from figure 3.5. A flow recirculation close to the hub at the measured outlet axis prevented obtaining experimental data for low mass flow in that region.

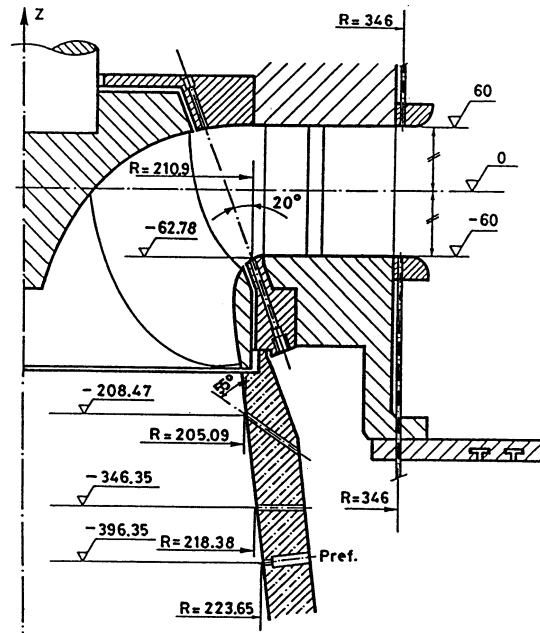


Figure 3.3: Geometrical and flow survey definitions. Picture taken from the GAMM Proceedings.

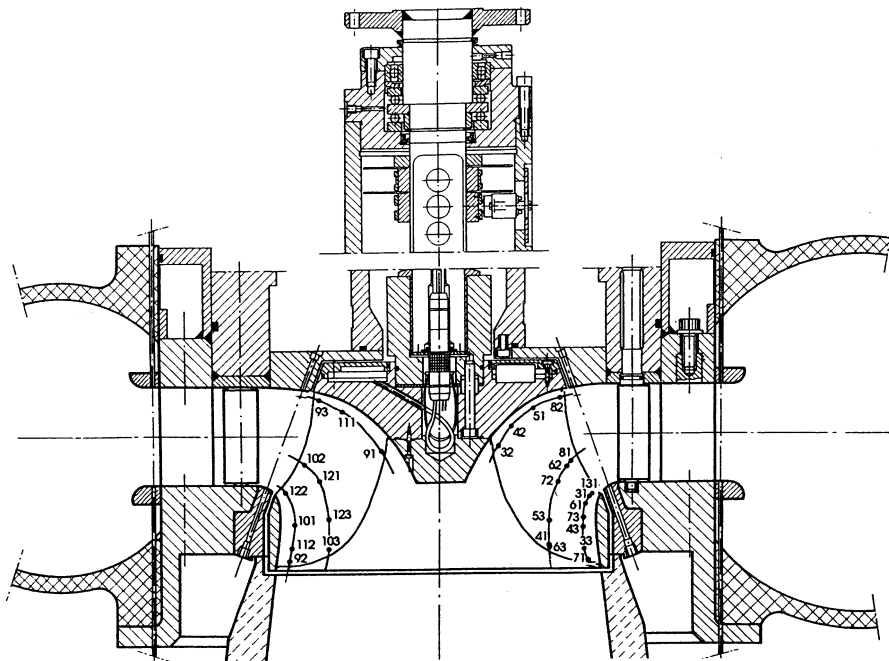


Figure 3.4: Pressure transducers. Picture taken from the GAMM Proceedings.

Operating condition	φ	ψ	η
1	0.286	1.07	0.920
2	0.220	0.66	0.850
3	0.330	1.40	0.910
4	0.220	1.07	0.885
5	0.330	1.07	0.905

Table 3.1: Operating conditions.

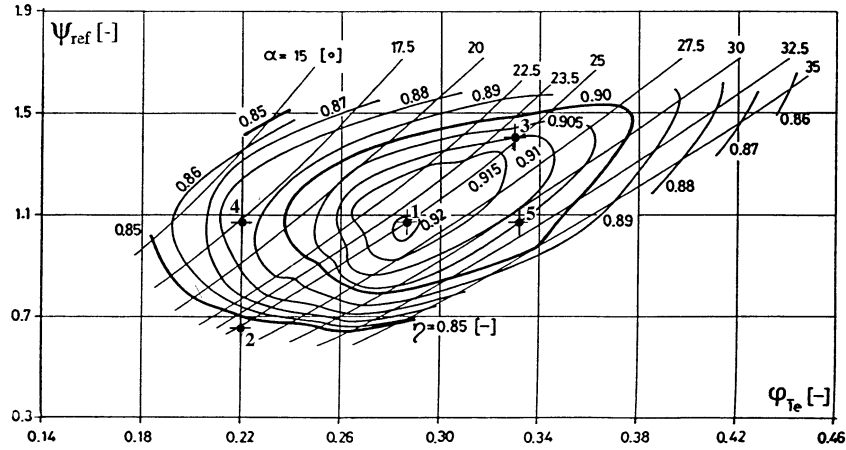


Figure 3.5: Operating conditions / hillchart. Modified picture from the GAMM Proceedings.

3.2.3 Remarks on the measurements

The databases were not as complete and the original off-design measurement files could not be found at the time of this work, and it was thus necessary to recover the measurements from the earlier computational validations made by Gros *et al.* [7]. Because of differences in normalizations, the curvilinear abscissa of the off-design pressure transducer measurements partly vanished. This was recovered by using the curvilinear abscissa of the pressure transducers in the ERCOFTAC description. Some of the static pressure measurements at streamline 2 are quite strange, however, and it may be that they are not correct. The curvilinear abscissa of the best efficiency operating point flow survey measurements also partly vanished. For instance, the measurements indicate absolute velocities at stationary walls.

The specific energy, E , was measured using two different downstream sections (figure 3.6), at the outlet of the draft tube (\bar{I}) according to the IEC standard and at the reference section ($\bar{2}$). The reason for this was the poor draft tube behaviour, which produced a hill chart with two peaks when the IEC standard was used. The new definition increased the best efficiency by about 2%. It would be desirable to have a better normalization factor than the specific energy, since it seems so difficult to specify exactly.

The torque and efficiency of the turbine were most likely measured for all operating conditions, but it has only been possible to recover them for the best efficiency operating condition. The efficiency of the off-design conditions is taken visually from the hill chart. However, the best efficiency measurement is not consistent with the corresponding torque, specific energy and volume flow measurements. The normalized torque in the proceedings is $t^* = 0.25577$. The definitions of the normalized torque, efficiency, energy coefficient and volume flow coefficient in the proceedings give an efficiency of $\eta = t^*/\varphi = 0.894$. This makes the efficiency

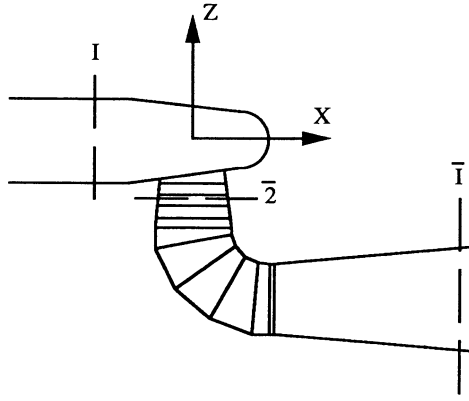


Figure 3.6: Schematic view of the turbine showing the reference sections between which the specific energy is measured. Picture taken from the GAMM Proceedings.

measurements more or less unreliable.

Avellan *et al.* [1] argued that the distributor inlet flow was constant all along the periphery and there were no differences between measurements at different runner inlet probe passages, which validates axisymmetric inlet conditions. However, later in the proceedings, it is argued that the measurements at the stay ring inlet show non-uniformities in the circumferential direction caused by an improper design of the spiral casing. For the computations in this work and for computations found in the literature on the GAMM turbine, the inlet distribution is assumed to be axis-symmetric.

The integrated volume flow from the measured velocity distributions does not give the same volume flow as specified. For the best efficiency operating point, the measured flow differs from the integrated measured velocity distributions by 7%. This may have its origin in non axis-symmetry of the flow, the velocity measurement error or the normalization error, for instance. In most of the comparisons between computed and measured velocity distributions, the integrated volume flow does not agree with what was reported in the experiments. The mass continuity of the computations is satisfied throughout the computational domain.

The GAMM Francis runner is also used for the ERCOFTAC workshop, where the measurements are made at somewhat different operating conditions.

The computational results are validated against the measurements recovered from the GAMM workshop and the data files from the preparations of the paper by Gros *et al.* [7]. The available data are sufficient for a detailed qualitative comparison.

Op. cond.	$E_{computed}$	$E_{measured}$	$t_{computed}^*$	$t_{measured}^*$	$\eta_{computed}$	$\eta_{measured}$
1	60.6	58.4	0.271	0.256/0.263	0.958	0.920
2	36.6	36.2	0.208	0.187	0.948	0.850
3	81.3	76.8	0.306	0.300	0.926	0.910
4	61.5	58.7	0.208	0.195	0.919	0.885
5	60.4	58.7	0.315	0.299	0.954	0.905

Table 4.1: Comparison of integral quantities.

4 Validation of the computational results

The computations are validated against the available measurements of the GAMM Francis runner in section 4.1. Some remarks on common numerical validations are made in section 4.2.

4.1 Experimental validation of the computational results

Both global measurements, such as specific energy, torque and efficiency, and detailed velocity and pressure measurements are used for the validation. Comparisons with global measurements are made in section 4.1.1, comparisons with detailed velocity and static pressure measurements are made in section 4.1.2 and comparisons with surface static pressure measurements are made in section 4.1.3.

4.1.1 Specific energy, torque and efficiency

The measured specific energy, $E_{measured}$, is measured between the inlet of the spiral casing and the cone reference section (see section 3.2.3). The computed specific energy, $E_{computed}$, is estimated by integration over the inlet and outlet of the computational domain, since the inlet of the spiral casing is not included in the computational domain. The computed specific energy is compared with the measured specific energy in table 4.1.

Note that the measured specific energy of the best efficiency operating point (Op. cond. 1) is slightly different than the measured specific energy of operating points 4 and 5. They are supposed to be the same. The measured specific energy of the best efficiency operating point is taken from the GAMM proceedings, while the rest are recovered from the work by Gros *et al.* [7]. It can be seen that the specific energy of the computations is slightly overestimated as compared with the measurements (or vice versa).

The computed torques and efficiencies are compared with experimental values in table 4.1. The measured torques for the off-design conditions are not available but are calculated from $t^* = \varphi\eta$. Note that the measured best efficiency torque from the GAMM proceedings (left) is not in accordance with what is calculated from the volume flow coefficient and the efficiency (right).

A quantitative comparison of the available data is difficult, since difficulties were encountered in defining the specific energy of the turbine. There are probably too many assumptions in the present definition of the specific energy and the results seem to be very dependent on how the measurements are carried out. Furthermore, in the present work, only part of the turbine is computed and the computed efficiency should thus be higher than the measured efficiency in the whole turbine.

4.1.2 Circumferentially averaged flow survey

Figures 4.1 - 4.5 compare the computed velocity profiles and flow angles with the measurements for each operating condition. The figures are all arranged with velocity comparisons to the left and flow angle comparisons to the right. The top figures are at the measured inlet axis, the center ones are at the measured middle axis and the lower are at the measured outlet axis. The measurement axes are described in section 3.2.1. The normalized abscissa, s , is defined as the distance from the shroud along the measurement axis, normalized by the reference radius, R_{ref} . The velocities are normalized with $\sqrt{2E}$ (since this was used for normalization of the measurements) and the angles are given in degrees. The markers are the measured values and the lines (composed of 50 evaluation points) are the circumferentially averaged computational results. Note that the lines do not go all the way to the boundaries.

At the measured inlet axis, one evaluation point of the circumferentially averaged results is in the hub boundary layer. That is why there is a sudden change in flow angles to the right in the graphs. Note that the hub is rotating; the tangential velocity coefficient is therefore non-zero at the hub. The definition of the meridional velocity, $C_m = \sqrt{C_r^2 + C_z^2}$, does not allow negative values. Thus, where back-flow occurs, the shapes of the meridional velocity coefficient and flow angle curves look odd (see e.g. figure 4.2(c-f)). As this definition of the meridional velocity is used in the GAMM and ERCOFTAC workshops, it is used here as well. It is easy to imagine what the curves would look like with a better definition, allowing negative values of the meridional velocity coefficient. The meridional velocity coefficient in the back-flow regions would then be mirrored about the x -axis. Since the definition of the flow angles is based on the meridional velocity, the same problem occurs in those graphs.

Note that the measured inlet axis is not the same as the inlet of the computational domain, which is described in section 2.3.3. The measured inlet axis velocity profiles has been extrapolated upstream to move the computational inlet away from the runner blades. The computed values at the measured inlet axis are thus strongly affected by the inlet boundary condition that is imposed. The computational results show that the velocity distributions agree fairly well with the measured profiles. Of course, modifying the inlet boundary conditions allows a much better agreement with the measurements at the measured inlet axis. The reason why this modification was not made is that the same extrapolation was used in the work by Gros *et al.* [7]. Furthermore, most hydraulic turbine computations do not have such detailed measurements with which to make comparisons. If the purpose of this work was to produce better runner inlet boundary conditions, separate distributor computations [14] or coupled computations would be done. That, however, is beyond the scope of this work.

The distribution of the meridional velocity is not uniform along the measured inlet axis (figure 4.1(a)) and, because of the curvature of the meridional contour of the turbine, the magnitudes of the meridional velocity generally increase at the lower ring and decrease at the upper ring. However, in the upper ring boundary layer, where the tangential velocity is the largest (figure 4.1(a)) and the effect of deceleration in the boundary layers due to friction becomes largest for the tangential velocity, the meridional velocity is accelerated, corresponding to a reduction in centrifugal force [8]. The tangential velocity distribution is relatively uniform.

Measurements of the middle axis (just after the runner) are available only for the best efficiency operating point. The computational results are very similar to the measurements for this case, see figure 4.1(c,d). It should be noted here that the computations satisfy mass conservation. Thus, the disagreement in the level between the computed and measured meridional velocity distribution must originate in non-periodicity of the experimental flow, in a normalization error or in measurement errors. The measurements are made at only one circumferential

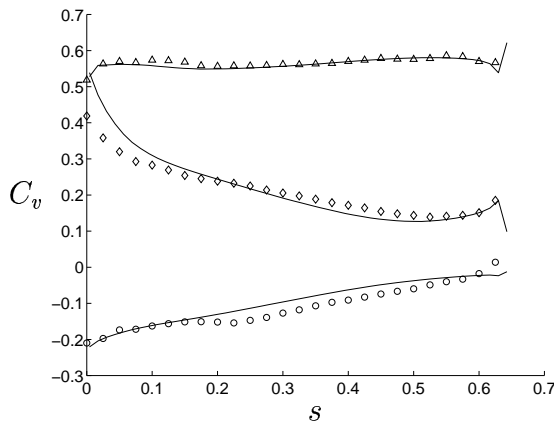
location, so the mass flow integrated from the measured meridional velocity contour does not have to give the true mass flow through the turbine. This discrepancy can be seen in most of the comparisons.

For best efficiency, the runner should be designed to give a uniform meridional velocity component and a zero tangential velocity component after the runner. The meridional flow at the measured middle axis is relatively uniform for operating points 1, 3 and 5. For the reduced flow operating points 2 and 4, there is a tendency toward recirculation at the hub. The tangential velocity distributions at the measured middle axis show a remaining swirl after the runner for all operating points. For operating points 3 and 5, the swirl changes sign at the center of the measured middle axis.

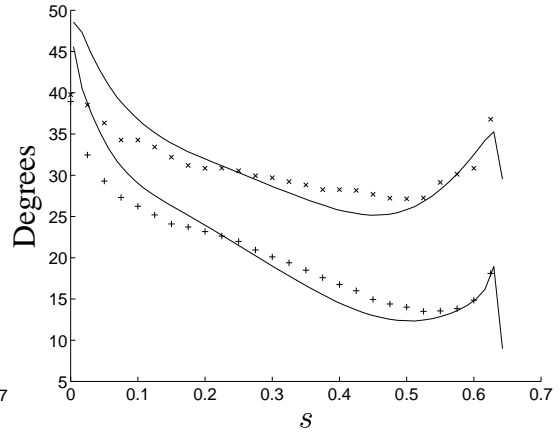
At the measured outlet axis, the length of the abscissa of the measurements at operating points 1, 3 and 5 is slightly longer than allowed by the geometry definition. A highly recirculating flow was found beneath the hub for operating points 2 and 4 during the measurements and, for this reason, measurements close to the axis of rotation were extremely difficult. There is thus a gap in the outlet axis measurements for these operating points. Because of the recirculation, the flow is highly transient in this region and stationary computations should fail to predict the flow since no steady solution exists. Convergence tests show that almost all the convergence problems during all computations had their origin in the flow beneath the hub. It is shown in section 4.2.1 that the flow beneath the hub, close to the axis of rotation, can be predicted differently for different initial fields. The flow at the outer part of the outlet axis was predicted the same, independently of initial field and further convergence.

Cobut *et al.* [3] draws a similar conclusion - that the runner outlet flow can be non-periodic and that recirculation at the outlet can lead to a lack of convergence, especially for low mass flow conditions (such as operating points 2 and 4). Such well-known instabilities of the flow can be clearly experimentally visualized by a cavitating vortex rope beneath the hub. This is one of the most interesting and challenging flow features in hydraulic machinery and should be studied numerically in the future. The comparisons still give a quantitative validation of the computational results, especially at the outer part of the measured outlet axis, where the meridional velocity is reduced because of the area change in the diffusor. To increase the flow prediction accuracy close to the rotational axis at the measured outlet axis, the flow between the blades close to the hub and at the separation at the end of the hub must be studied in detail. Most likely, the flow in this region requires the use of a transient solution procedure, without a periodic assumption.

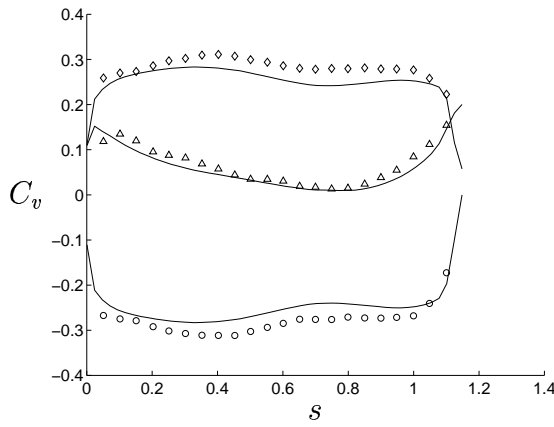
The flow in the vicinity of the runner is not axisymmetric. There are upstream effects from the runner because of the non-axisymmetric pressure distribution at the runner leading edge and downstream effects from the runner because of the wakes of the runner blades that are produced by the boundary layers and the bluff runner blade trailing edge. The non-axisymmetry is studied in figures 4.6 and 4.7. In these figures, the same results as presented earlier are presented together with the maximum and minimum of the velocity components along the circumference. The maximum and minimum values are displayed as dashed lines. Surprisingly, the non-axi-symmetry is very small. Particularly at the measured outlet axis, the computed flow is perfectly axisymmetric. This could perhaps be expected for the best efficiency operating point but, for operating point 2, with a recirculation tendency at the measured middle axis and strange outlet axis velocity profiles, the flow may be expected to be non-axisymmetric. However, the computed flow at the measured outlet axis is perfectly axisymmetric for operating point 2 as well. This may indicate that the computations are too dissipative so that the runner blade wakes disappear too soon or that the outlet boundary condition reduces the non-axi-symmetry. It is difficult to say anything about this, however, because, in this region, upstream effects from the



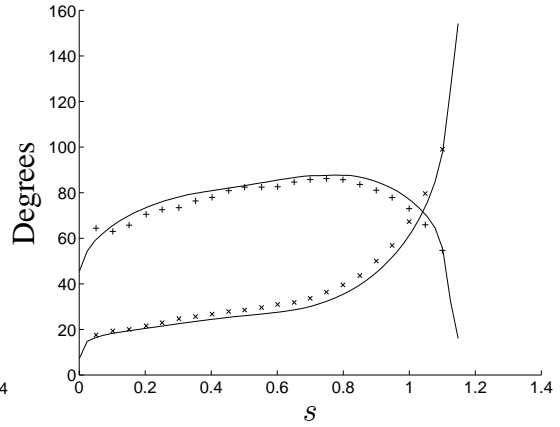
(a) Inlet axis absolute velocity coefficients.



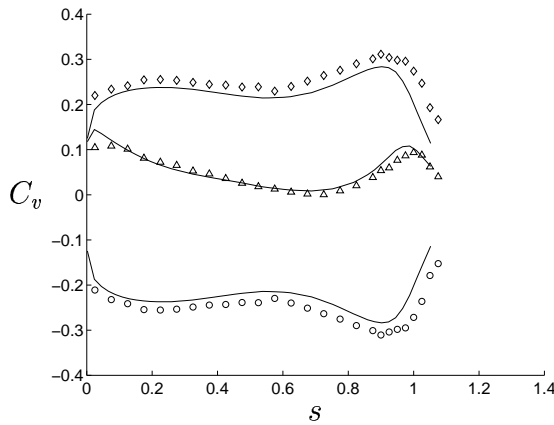
(b) Inlet axis flow angles.



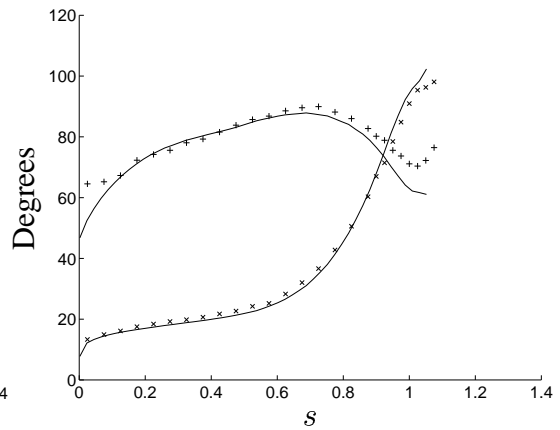
(c) Middle axis absolute velocity coefficients.



(d) Middle axis flow angles.

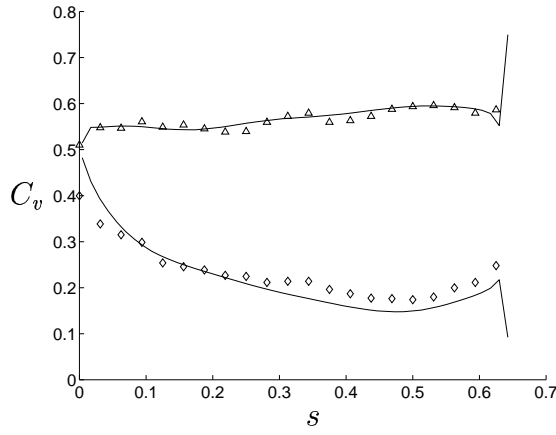


(e) Outlet axis absolute velocity coefficients.

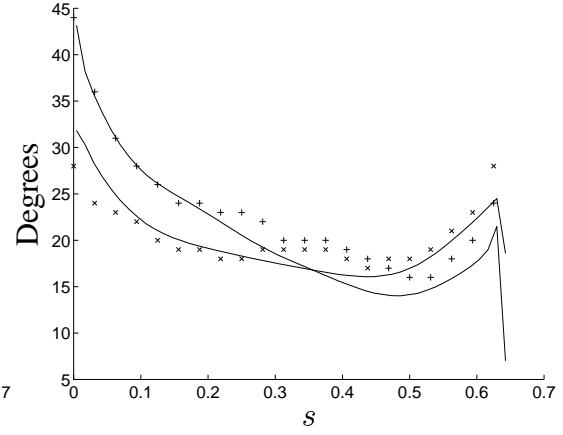


(f) Outlet axis flow angles.

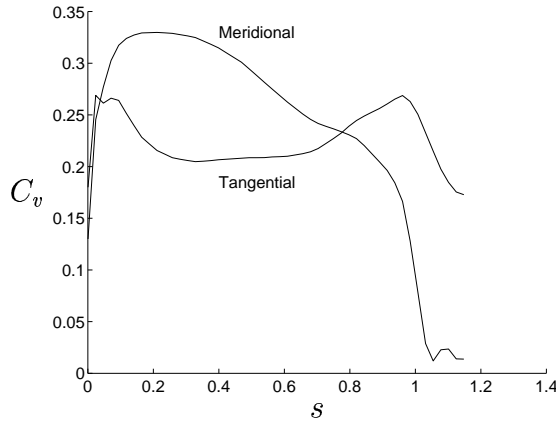
Figure 4.1: Operating point 1 flow survey. Solid lines: circumferentially averaged computational results. Measurement markers: \triangle : Tangential, \circ : Axial, \diamond : Meridional, $+$: Absolute (α), \times : Relative (β).



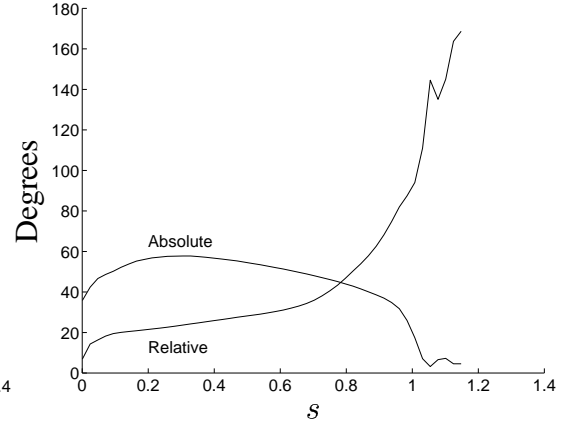
(a) Inlet axis absolute velocity coefficients.



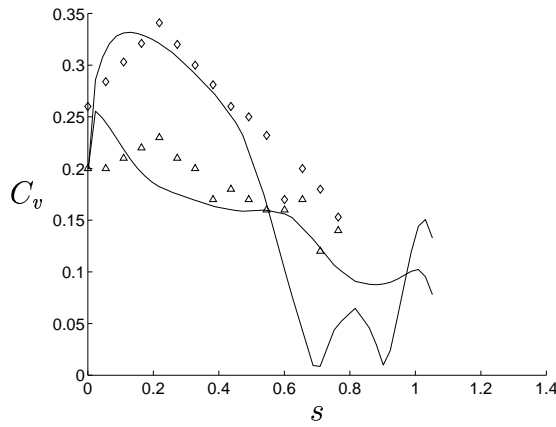
(b) Inlet axis flow angles.



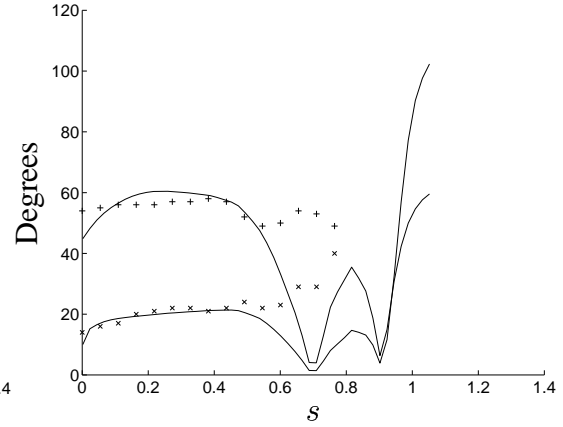
(c) Middle axis absolute velocity coefficients.



(d) Middle axis flow angles.

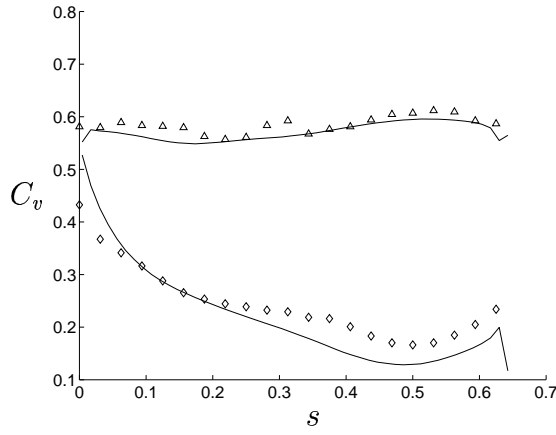


(e) Outlet axis absolute velocity coefficients.

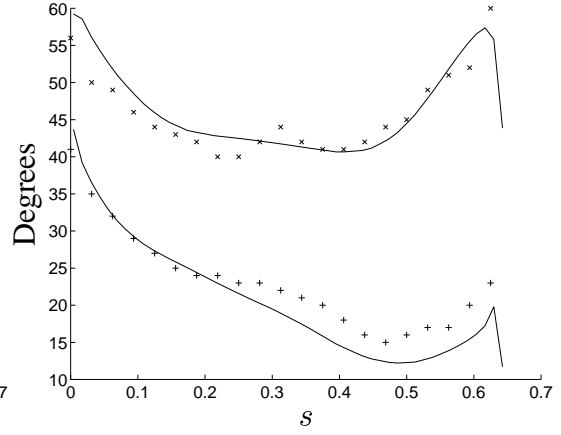


(f) Outlet axis flow angles.

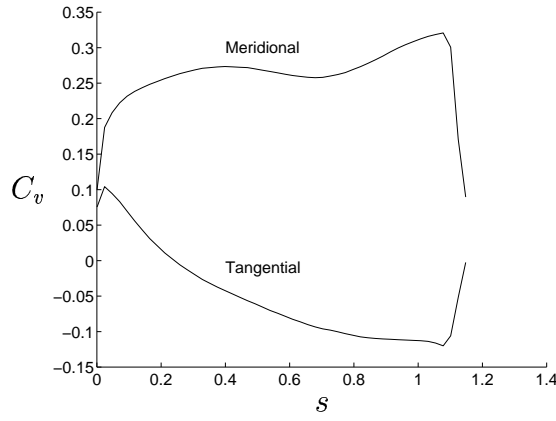
Figure 4.2: Operating point 2 flow survey. Solid lines: circumferentially averaged computational results. Measurement markers: \triangle : Tangential, \diamond : Meridional, $+$: Absolute (α), \times : Relative (β).



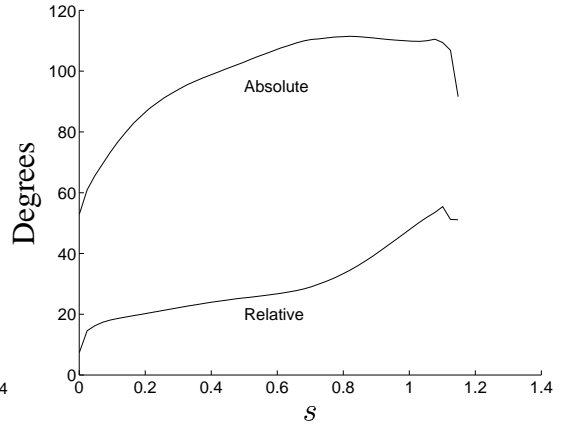
(a) Inlet axis absolute velocity coefficients.



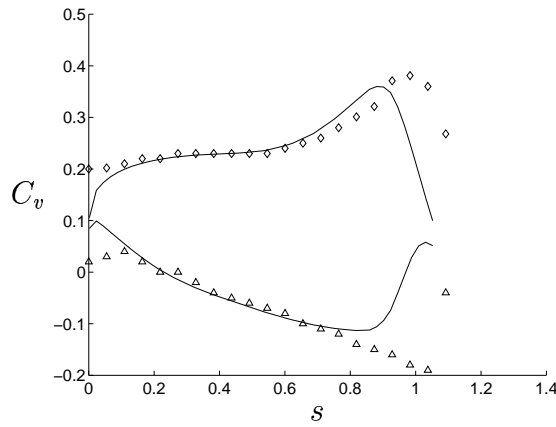
(b) Inlet axis flow angles.



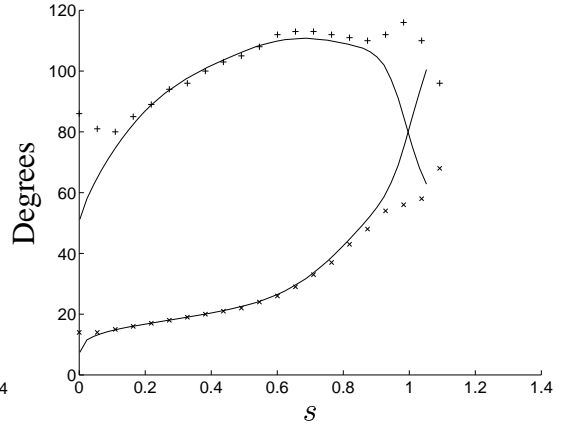
(c) Middle axis absolute velocity coefficients.



(d) Middle axis flow angles.

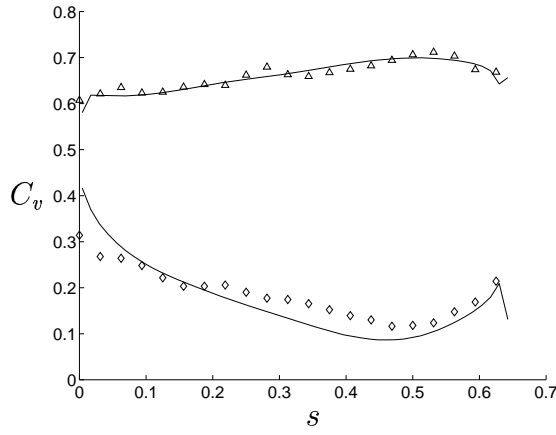


(e) Outlet axis absolute velocity coefficients.

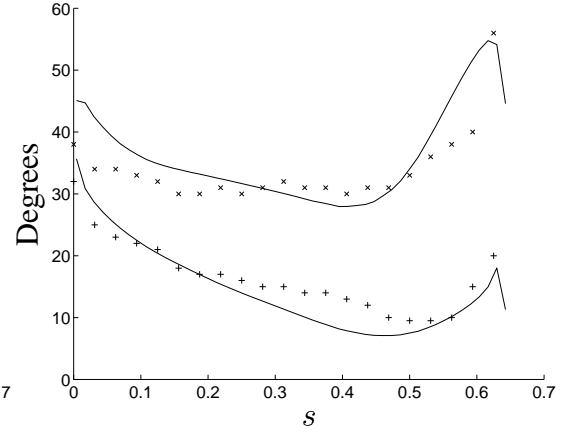


(f) Outlet axis flow angles.

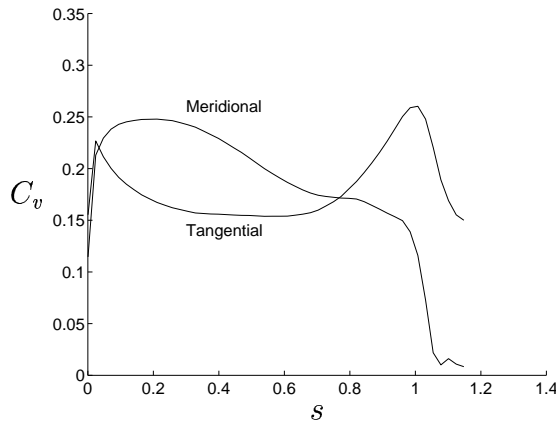
Figure 4.3: Operating point 3 flow survey. Solid lines: circumferentially averaged computational results. Measurement markers: \triangle : Tangential, \diamond : Meridional, $+$: Absolute (α), \times : Relative (β).



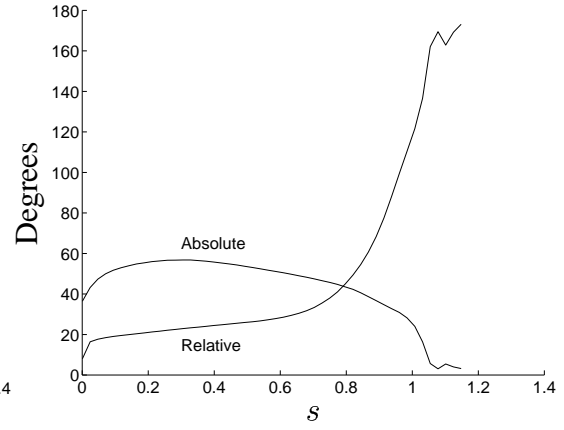
(a) Inlet axis absolute velocity coefficients.



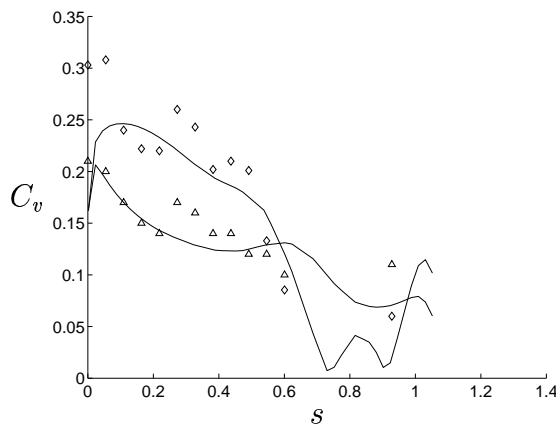
(b) Inlet axis flow angles.



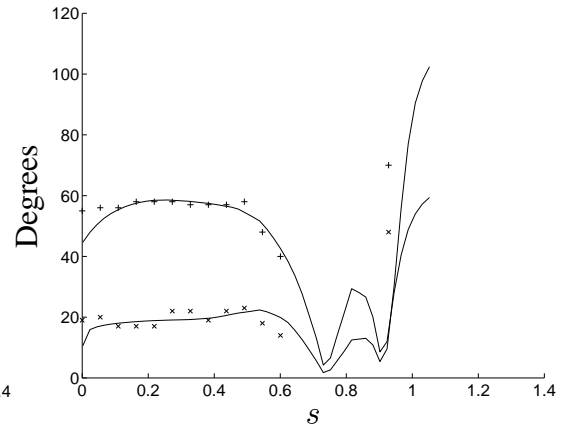
(c) Middle axis absolute velocity coefficients.



(d) Middle axis flow angles.

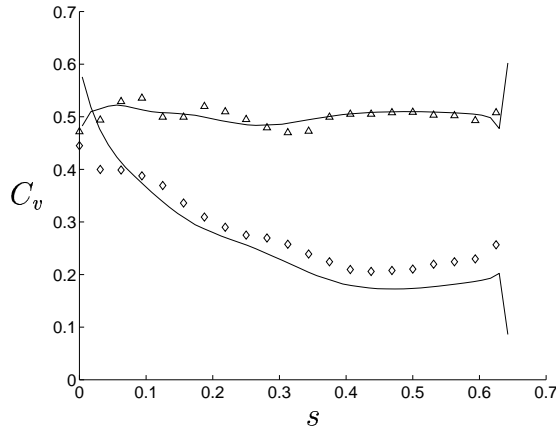


(e) Outlet axis absolute velocity coefficients.

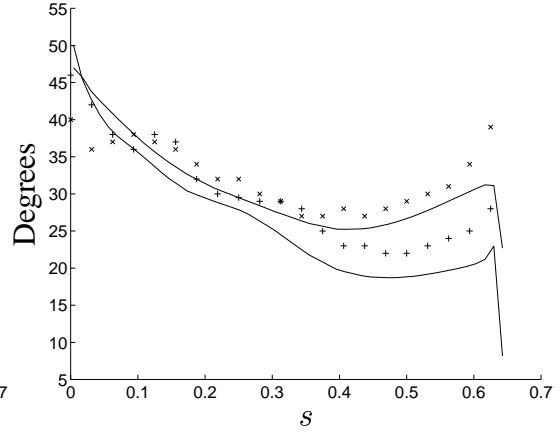


(f) Outlet axis flow angles.

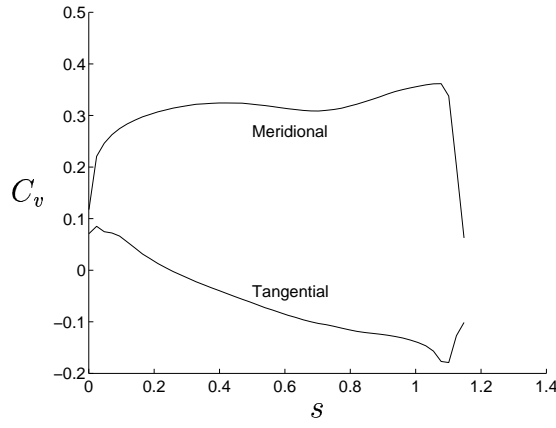
Figure 4.4: Operating point 4 flow survey. Solid lines: circumferentially averaged computational results. Measurement markers: \triangle : Tangential, \diamond : Meridional, $+$: Absolute (α), \times : Relative (β).



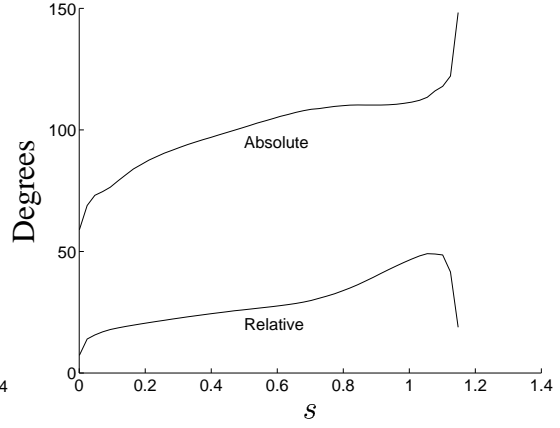
(a) Inlet axis absolute velocity coefficients.



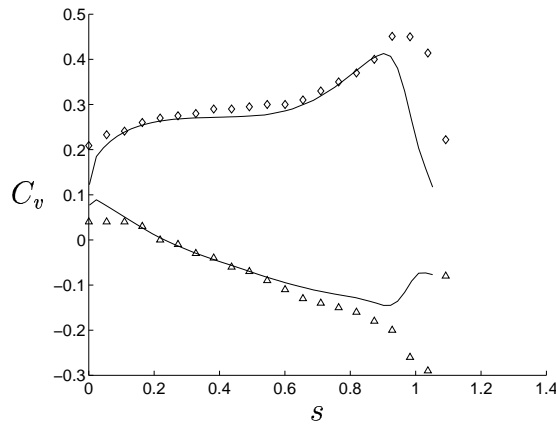
(b) Inlet axis flow angles.



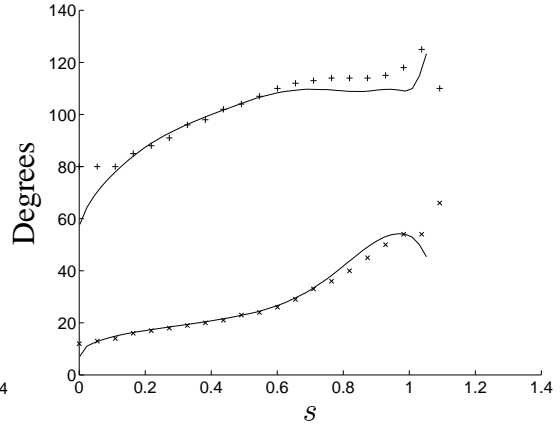
(c) Middle axis absolute velocity coefficients.



(d) Middle axis flow angles.



(e) Outlet axis absolute velocity coefficients.



(f) Outlet axis flow angles.

Figure 4.5: Operating point 5 flow survey. Solid lines: circumferentially averaged computational results. Measurement markers: \triangle : Tangential, \diamond : Meridional, $+$: Absolute (α), \times : Relative (β).

draft tube will influence the flow and the flow is nevertheless highly transient and non-periodic.

Measurements of the static pressure distribution at the measured outlet axis are available only for the best efficiency operating point. The static pressure distribution for this operating point is well predicted by the computations (figure 4.8(a)). For the other operating conditions, figure 4.8 show that operating points 1, 3 and 5 have similar pressure distribution and operating points 2 and 4 have similar pressure distribution. As shown in the velocity distributions, operating points 1, 3 and 5 have a strong vortex at the axis, while operating points 2 and 4 have a less strong vortex at the axis with recirculation and unsteadiness. Operating points 2 and 4 have lower pressure distributions than operating points 1, 3 and 5. Vortex rope cavitation behaviour beneath the hub is not described in the measurement paper [1], but it is reasonable to believe that there are highly unsteady cavitating vortex ropes for operating points 2 and 4 in high settings. A picture of the vortex rope (in the measurement paper) for a high setting of the best efficiency operating point shows that the vortex rope for that operating point is very straight and thus qualitatively steady (figure 4.9).

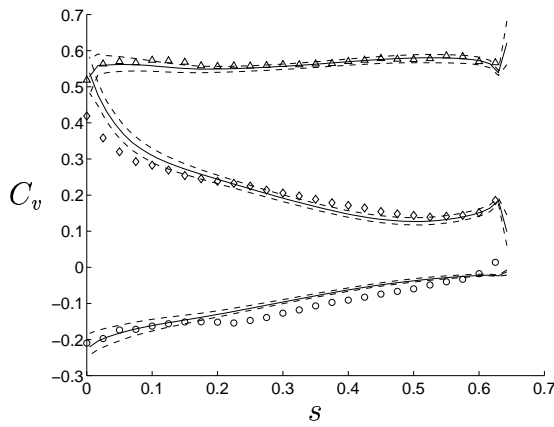
4.1.3 Runner blade static pressure distribution

The distribution of the computed static pressure coefficient along two profiles of the runner blades is compared with measurements in figures 4.10 to 4.14. The profiles correspond to 'theoretical streamlines' numbers 2 and 15 in the proceedings of the GAMM workshop [1]. The profiles are described in figure 3.4 in section 3.2.1, where profile 2 is close to the hub and profile 15 is close to the shroud. Profile 9 (mid-channel) is also shown, but no off-design measurements are available for that profile. The measured pressure distribution used for comparison in this work is taken from the work of Gros *et al.* [7]. Owing to unknown normalization of the measured data, the positions of the transducers were lost in the available data. The positions of the transducers were recovered by comparing the available data with the specifications in the ERCOFTAC description [15]. Since the pressure transducers are not exactly placed at the corresponding streamlines and because of interpolation problems, the computed results are displayed at the grid lines that best describe the measurement positions. The normalized abscissa, s , is the distance from the leading edge along the surface of the blade profile, normalized by R_{ref} .

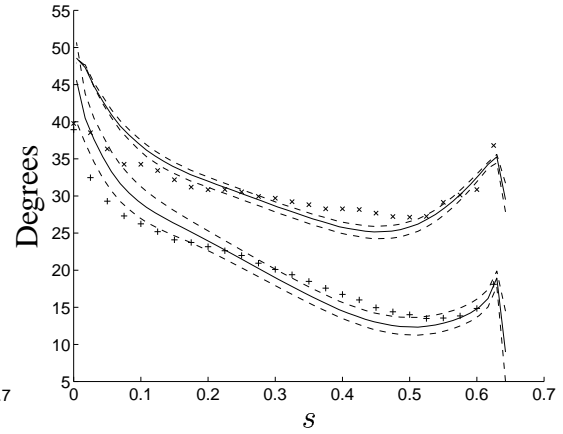
The computations give roughly the same distribution and blade loading as the measurements for profile 15. The low pressure peaks at $s = 0.1$ at the suction side are however not captured (as distinctly as in the measurements) by the computations. The predicted pressure distribution in the blade passage however clearly shows a region of reduced pressure in this region (see section 5.3). In the measurements [1], cavitation owing to the reduced pressure had its origin in this region (figure 4.15). The computational results for profile 2 do not show the same similarity with the measurements as for profile 15. The main features of the pressure distribution are recovered, but the blade loading distribution is not the same. However, it is questionable whether the blade loading is actually as low as indicated by the measurements.

4.2 Numerical validation of the computational results

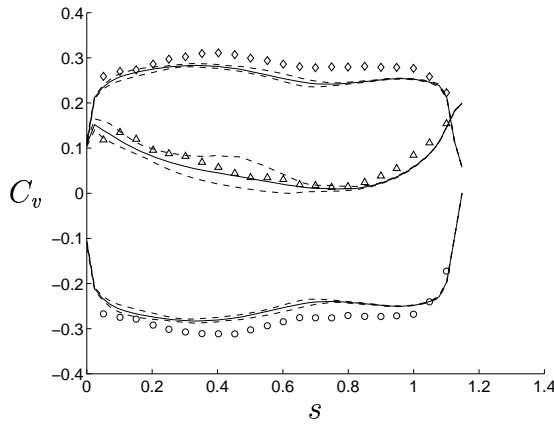
The computational results in this work show great similarity with the computational results from the TASCflow CFD code, which produced the best results of the codes used for the computations in Gros *et al.* [7]. It was argued, however, that the N3S CFD code was able to better predict a low pressure peak on the suction side near the leading edge and close to the shroud, where cavitation development was observed during the experiments. In the runner blade static pressure



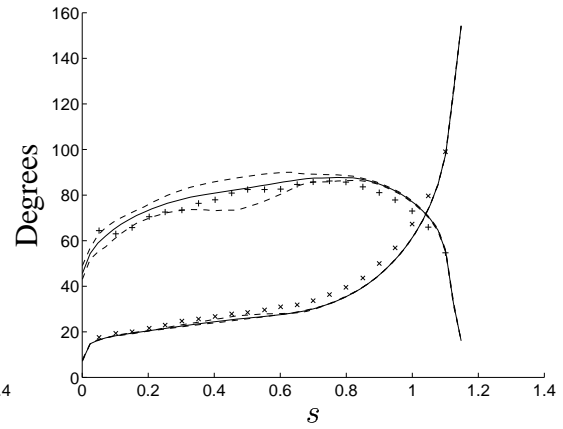
(a) Inlet axis absolute velocity coefficients.



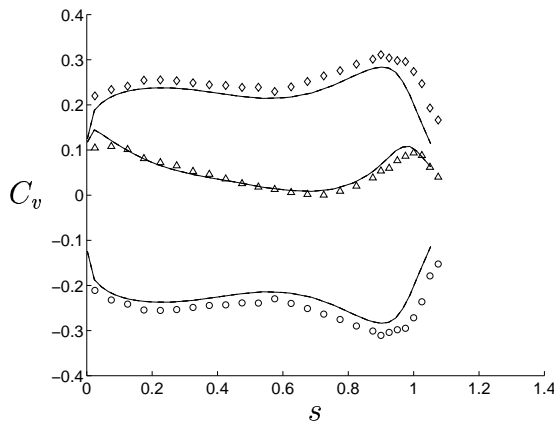
(b) Inlet axis flow angles.



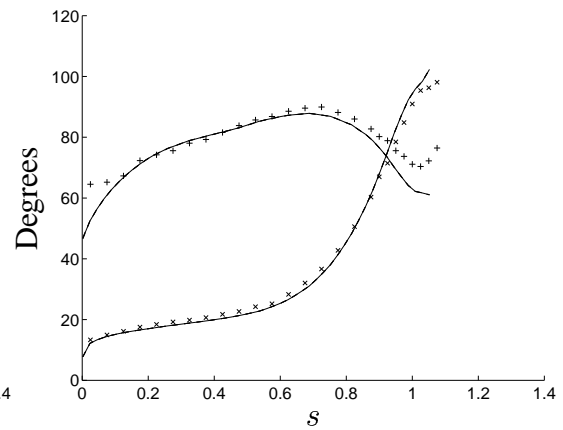
(c) Middle axis absolute velocity coefficients.



(d) Middle axis flow angles.

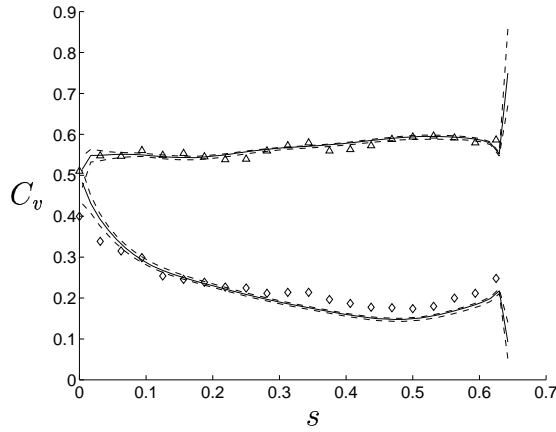


(e) Outlet axis absolute velocity coefficients.

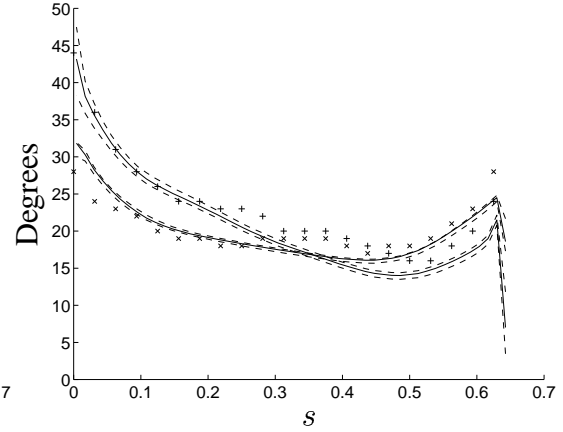


(f) Outlet axis flow angles.

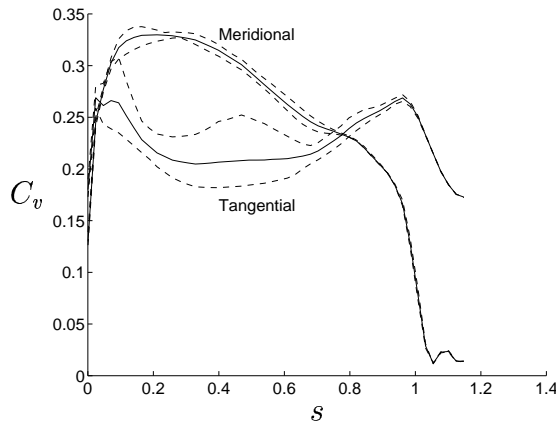
Figure 4.6: Operating point 1 flow survey. Solid lines: circumferentially averaged computational results (Dashed lines show minimum and maximum values). Measurement markers: \triangle : Tangential, \circ : Axial, \diamond : Meridional, $+$: Absolute (α), \times : Relative (β).



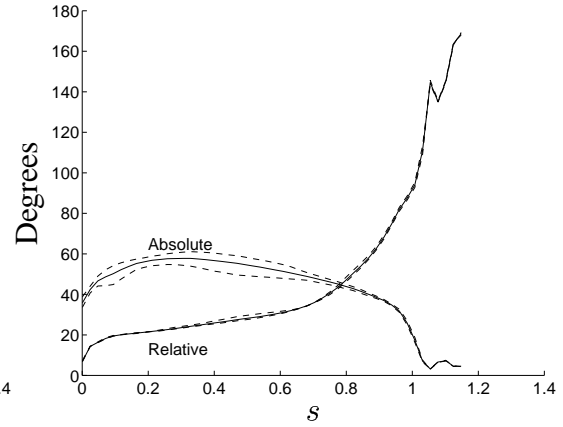
(a) Inlet axis absolute velocity coefficients.



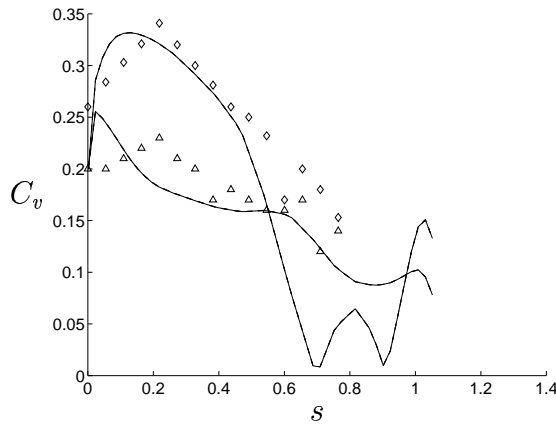
(b) Inlet axis flow angles.



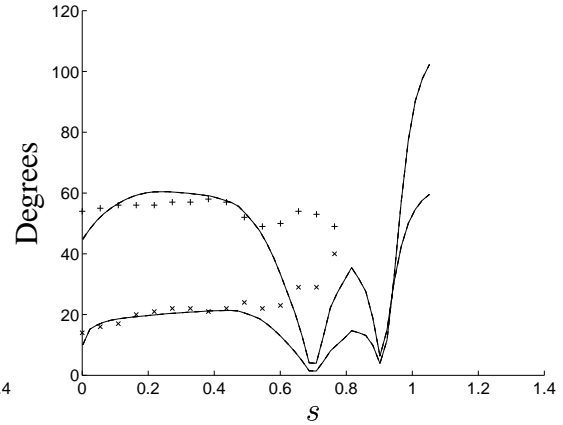
(c) Middle axis absolute velocity coefficients.



(d) Middle axis flow angles.

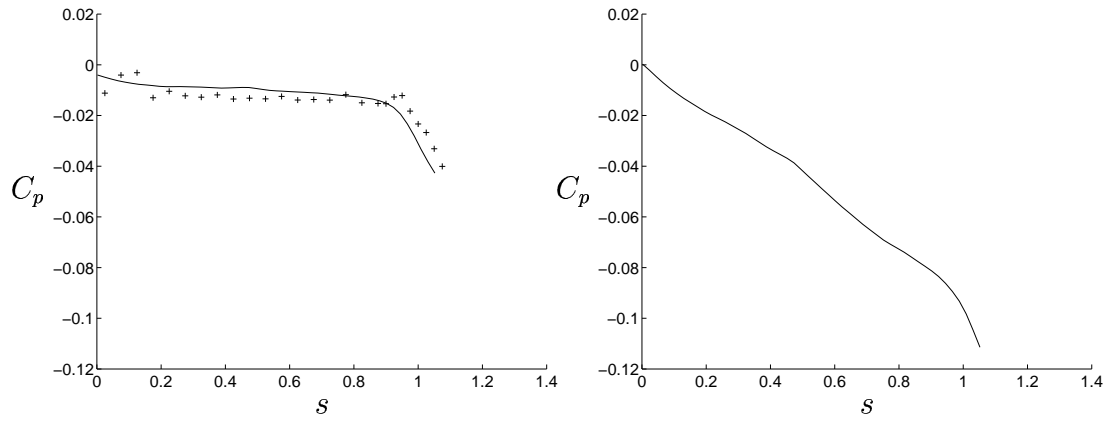


(e) Outlet axis absolute velocity coefficients.



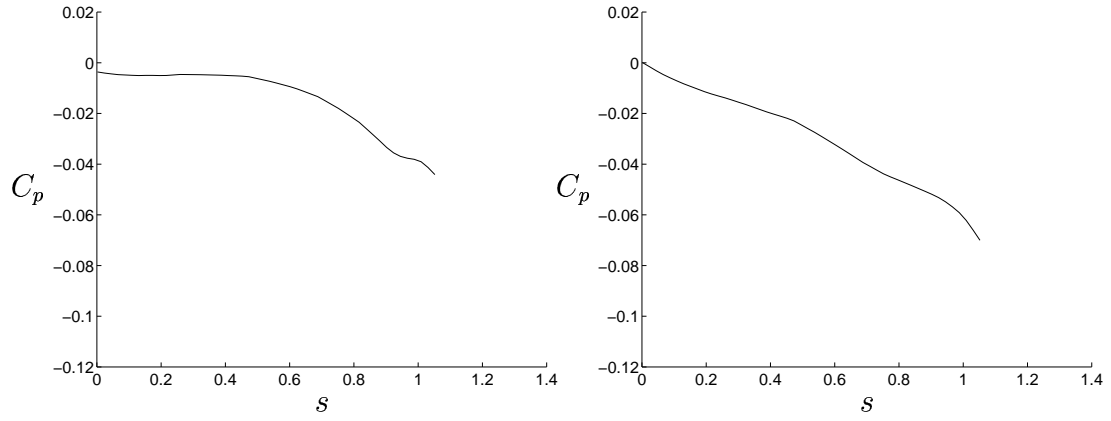
(f) Outlet axis flow angles.

Figure 4.7: Operating point 2 flow survey. Solid lines: circumferentially averaged computational results (Dashed lines show minimum and maximum values). Measurement markers: \triangle : Tangential, \diamond : Meridional, $+$: Absolute (α), \times : Relative (β).



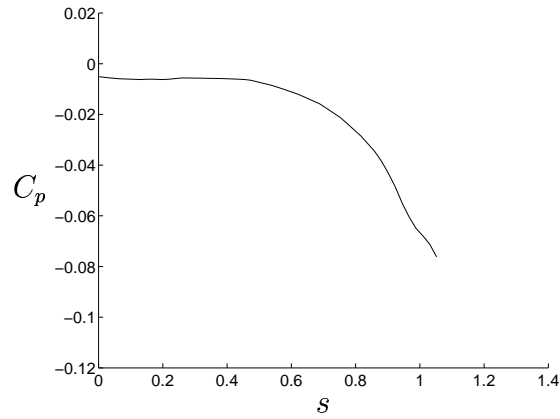
(a) Operating point 1.

(b) Operating point 2.



(c) Operating point 3.

(d) Operating point 4.



(e) Operating point 5.

Figure 4.8: Outlet axis static pressure distribution. Solid lines: circumferentially averaged computational results, +: measurements.

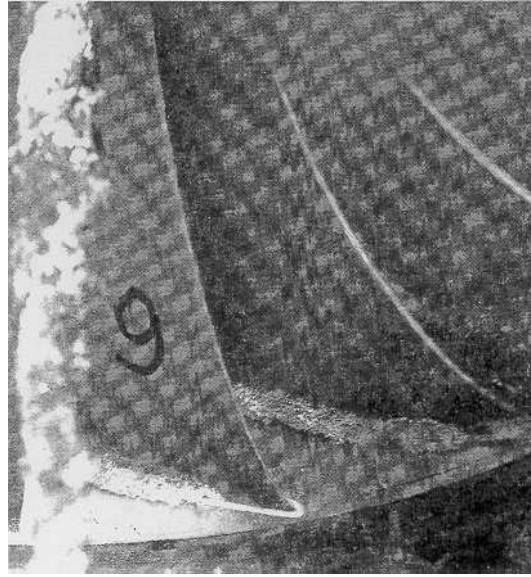


Figure 4.9: Photography of the inlet edge cavitation development and vortex rope behaviour at the best efficiency operating point. Picture taken from the GAMM Proceedings.

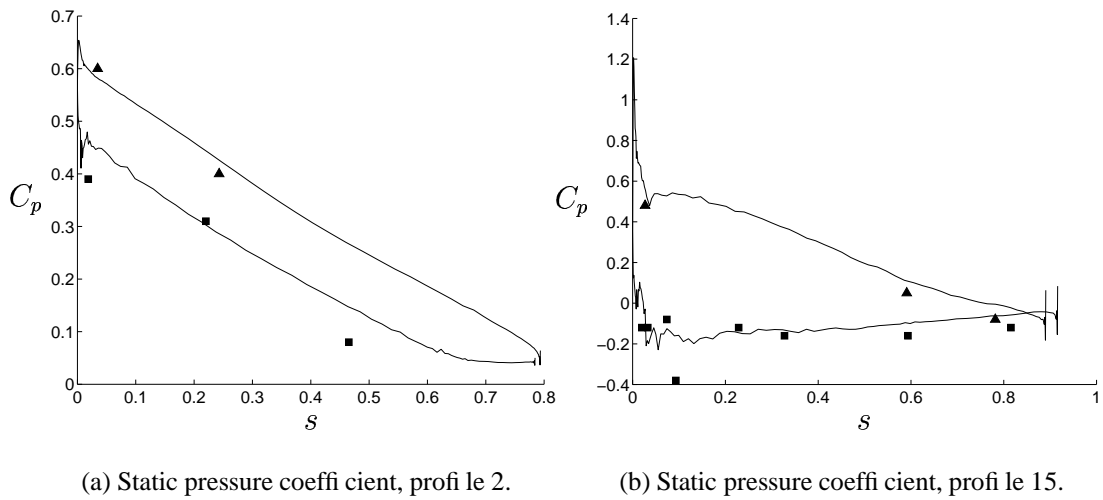
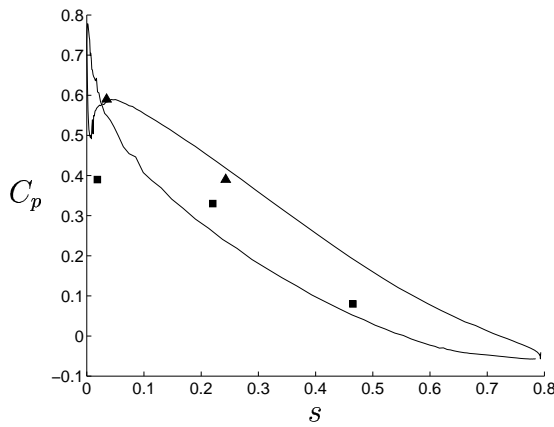
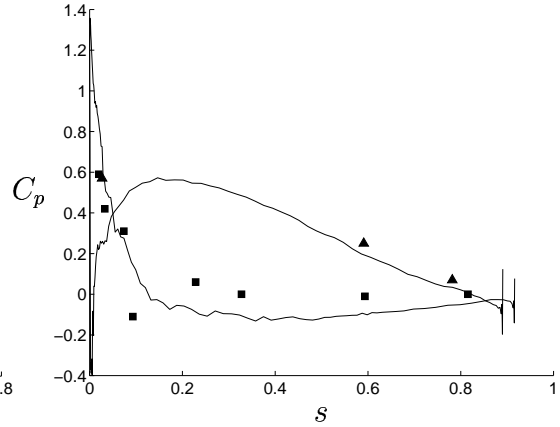


Figure 4.10: Runner surface static pressure coefficient, operating point 1. Solid lines: computational results. Measurement markers: \blacktriangle : Pressure side, \blacksquare : Suction side.

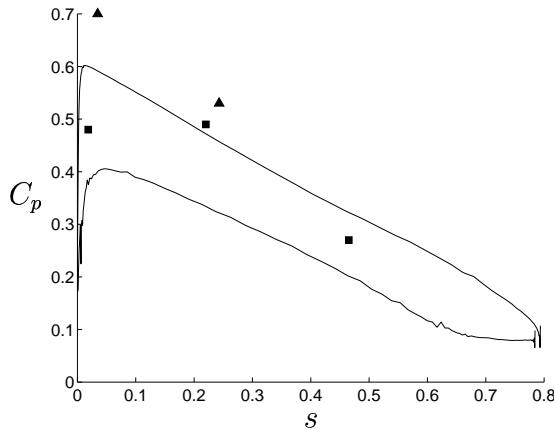


(a) Static pressure coefficient, profile 2.

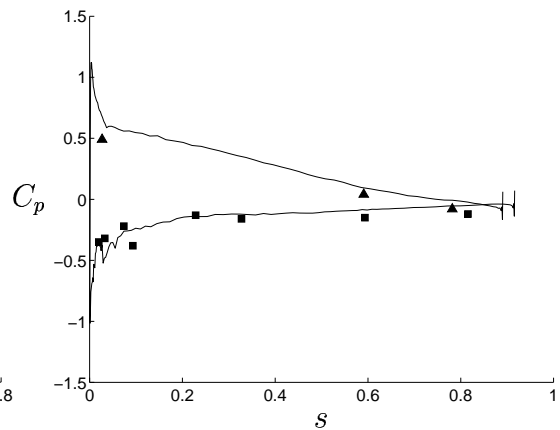


(b) Static pressure coefficient, profile 15.

Figure 4.11: Runner surface static pressure coefficient, operating point 2. Solid lines: computational results. Measurement markers: ▲: Pressure side, ■: Suction side.

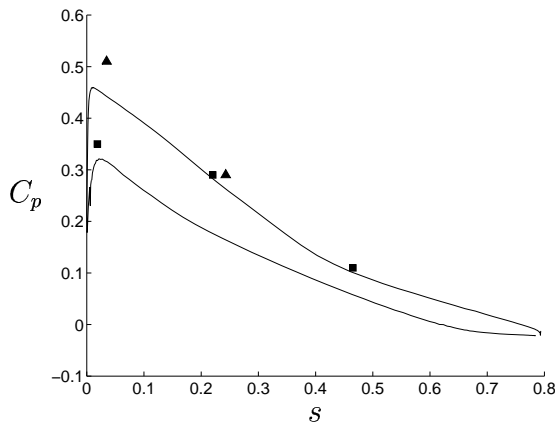


(a) Static pressure coefficient, profile 2.

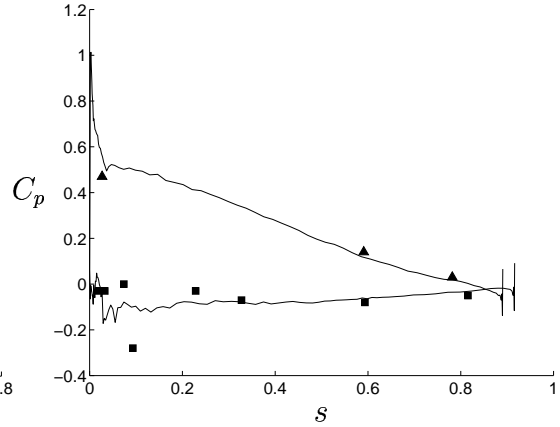


(b) Static pressure coefficient, profile 15.

Figure 4.12: Runner surface static pressure coefficient, operating point 3. Solid lines: computational results. Measurement markers: ▲: Pressure side, ■: Suction side.

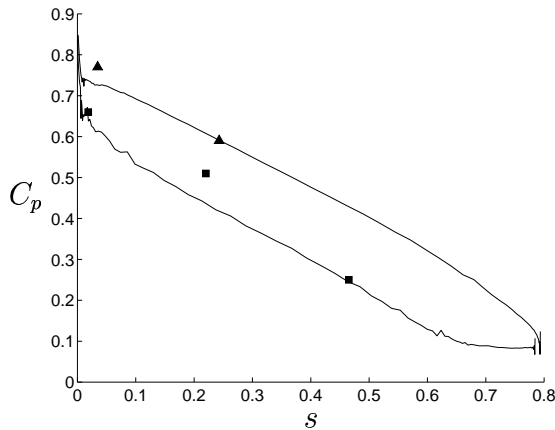


(a) Static pressure coefficient, profile 2.

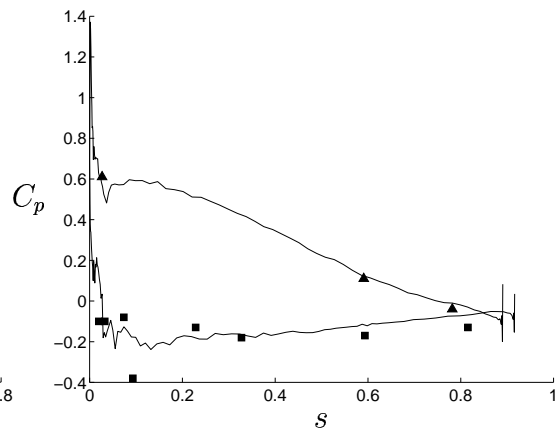


(b) Static pressure coefficient, profile 15.

Figure 4.13: Runner surface static pressure coefficient, operating point 4. Solid lines: computational results. Measurement markers: \blacktriangle : Pressure side, \blacksquare : Suction side.



(a) Static pressure coefficient, profile 2.



(b) Static pressure coefficient, profile 15.

Figure 4.14: Runner surface static pressure coefficient, operating point 5. Solid lines: computational results. Measurement markers: \blacktriangle : Pressure side, \blacksquare : Suction side.



Figure 4.15: Photograph of the inlet edge cavitation development at the best efficiency operating point. Picture taken from the GAMM Proceedings.

distributions presented in this work (section 4.1.3), this low pressure peak is not clear, although can readily be observed by using an iso-surface of low static pressure (section 5.3).

When making numerical simulations, it must be ensured that the residuals of the computed equations and the continuity error are small. It should also be checked that special requirements such as the first node y^+ value are sufficiently good. This is done in the following sections.

4.2.1 Convergence

Computations are commonly assumed to be converged when the largest non-dimensional residual of the momentum and continuity equations is reduced to 10^{-3} . The residuals of the discretized momentum equations are non-dimensionalized by $(\dot{m} + \dot{m}_{rel})W_{max}$, and the residual of the discretized continuity equation is non-dimensionalized by $(\dot{m} + \dot{m}_{rel})$, where \dot{m}_{rel} is the rotational mass flow through the periodic boundaries, \dot{m} is the mass flow through the runner and W_{max} is the largest *relative* velocity in the computational domain. For the computations in this work, the largest non-dimensional residual was reduced to between $5.5 \cdot 10^{-5}$ and $8.5 \cdot 10^{-4}$, the worst of them being for operating points 2 and 4 which have recirculation under the hub.

Convergence tests show that almost all the convergence problems during all computations had their origin in the flow beneath the hub. Figure 4.16 compares the measured outlet axis absolute velocity coefficients for two computations of operating point 5 with measurements. The difference between the computations is the initial field for the tangential velocity. For one of the computations, the results from the best efficiency operating point were used as a initial field while for the other computation, the results from the best efficiency operating point with a modified tangential velocity distribution were used as a initial field. The initial tangential velocity coefficient distributions for the two cases (in the region of the measured outlet axis) were $\overline{C_u} \approx 0.1$ and $C_u = -0.1$, respectively. The computational results converged to exactly the same results in all the computational domain except under the hub, where the convergence is too slow, especially for the tangential component. The discrepancy in this region is probably

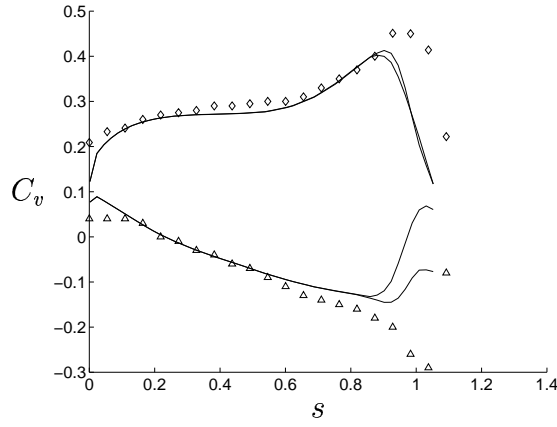
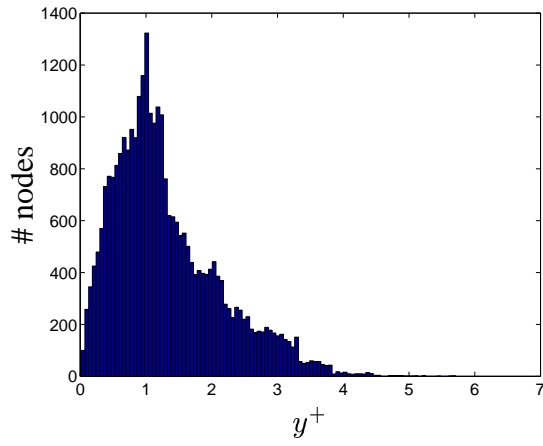


Figure 4.16: Outlet axis absolute velocity coefficients. Convergence problems under the hub. Solid lines: circumferentially averaged computational results. Measurement markers: \triangle : Tangential, \diamond : Meridional.

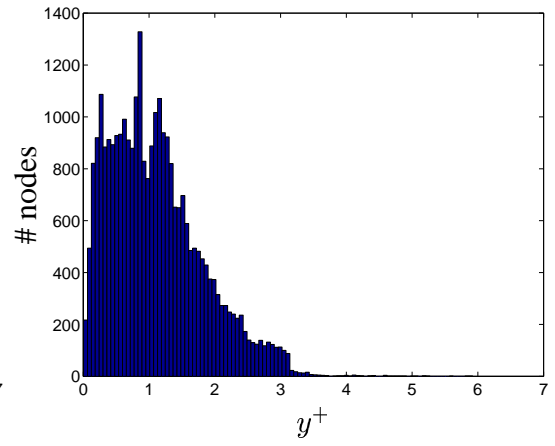
not very important for the overall computed behaviour of the runner, but it would be interesting to investigate this further. That is however beyond the scope of this work.

4.2.2 Low Reynolds wall treatment

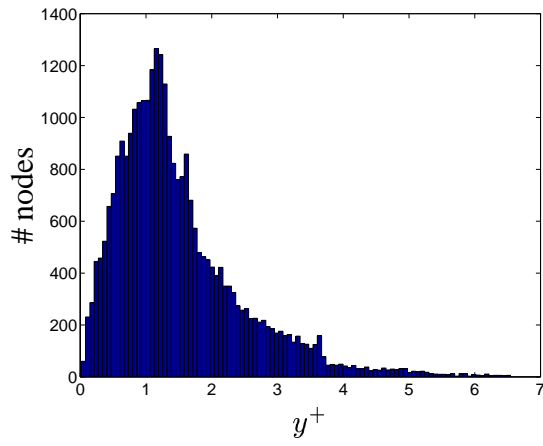
For low Reynolds turbulence models such as the $k - \omega$ [18] model used for the computations in this work, the first node inside a wall should be placed in the viscous sub-layer ($y^+ < 5$). Wilcox proposes that the boundary condition for ω (equation 2.1) should be applied for at least 5 nodes between $0 < y^+ < 2.5$, with the first node below $y^+ = 1$. However, the relative flow in a water turbine runner is highly accelerating, yielding very thin boundary layers. There are also stagnation points at the runner blade leading edges, where the boundary layer starts to develop. Because of this and the probably small impact on the flow, placing the first node in the viscous sub-layer is assumed to be sufficient. Figure 4.17 shows histograms of the distribution of the first node y^+ values. Most of the first node y^+ values are thus below 1.5 for all computations.



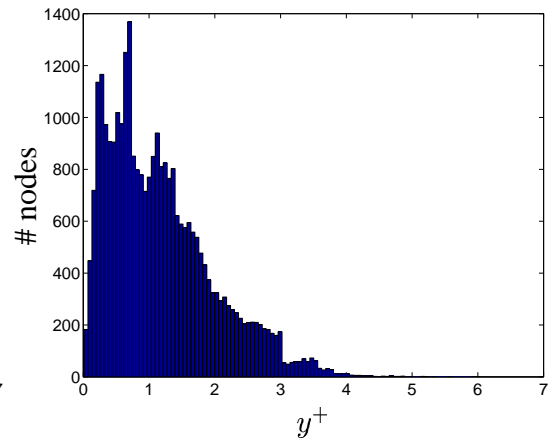
(a) Operating point 1.



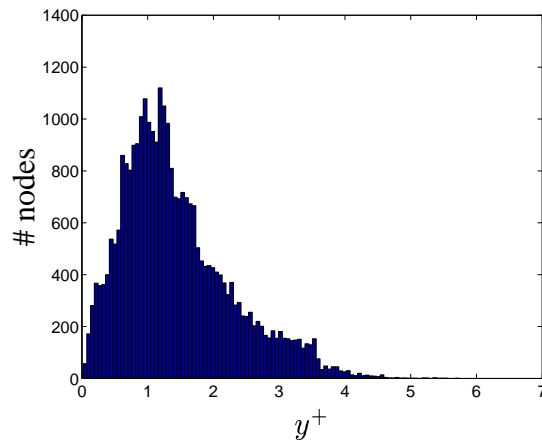
(b) Operating point 2.



(c) Operating point 3.



(d) Operating point 4.



(e) Operating point 5.

Figure 4.17: Distribution of near-wall y^+ values.

5 Flow feature visualization

In the computations, a periodic assumption reduces the computational domain to 1/13th of the original size. Some post-processing tools, such as Enight, have rotational periodic treatment. However, during this work, one periodic part of the domain contains 560 736 control volumes. With 13 runner blades, the complete model contains 7 289 568 control volumes. This is far too much for the facilities used for this work. A reduction of the computational results is necessary but is not sufficient if most of the detailed flow features must be visualized. Thus, the whole computational domain cannot be visualized at the same time. The solution to this problem is to visualize the computational results in one part of the domain, save the results as unstructured geometry and re-load them into a rotational periodic coordinate system. In this way, it looks like all the results have been periodically rotated, while only a very small fraction of it actually has. In the following sections, some of the computational results are visualized to show some of the features of the flow that were captured by the computations.

5.1 Streamlines

There is a recirculation region beneath the hub for low mass flow. This is a region of unsteadiness for these operating conditions. This unsteadiness cannot be captured using stationary periodic computations. Furthermore, the draft tube is not included in the computations so the outlet boundary condition plays a major role with respect to recirculation. The computations can therefore not be expected to capture the outlet flow correctly for low mass flow. A comparison between operating conditions 1 and 2, which are the best and worst operating conditions in this context, is made in figure 5.1. Ten streamlines of the flow relative to the runner are used in both pictures. The streamlines are not allowed to go through the runner blade passages, since the visualization facilities did not allow all of the domain to be visualized at the same time. The streamlines follow the hub shape nicely for operating point 1, but there is a large region of recirculation for operating point 2. The recirculation region is cone shaped and extends from the outlet of the computational domain to the lower part of the hub. The recirculation flow is co-rotating with the main flow, which can also be seen in figure 4.2(e) in section 4.1.2. Some of the recirculating streamlines attach to the main flow and some attach to a small region of flow that circulates downwards along the rotational axis.

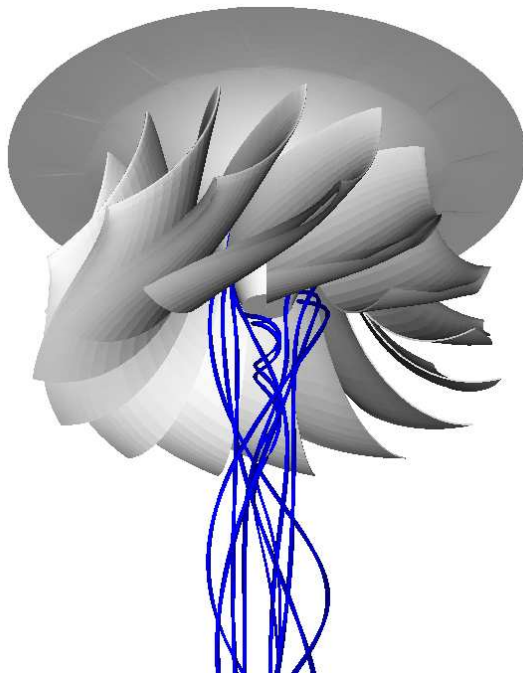
5.2 Surface static pressure distribution

The runner blade surface static pressure coefficient distributions for the studied operating conditions are shown in figure 5.2. Operating conditions 1, 3 and 5 have similar static pressure distributions, with a local static pressure reduction at the runner blade leading edge suction side, close to the band. Cavitation was observed in this region, for these operating conditions, during the experiments [1]. Operating conditions 2 and 4 have similar static pressure distribution, with a large static pressure reduction at the end of the hub. Recirculation and unsteadiness were observed in this region for these operating conditions during the experiments [1].

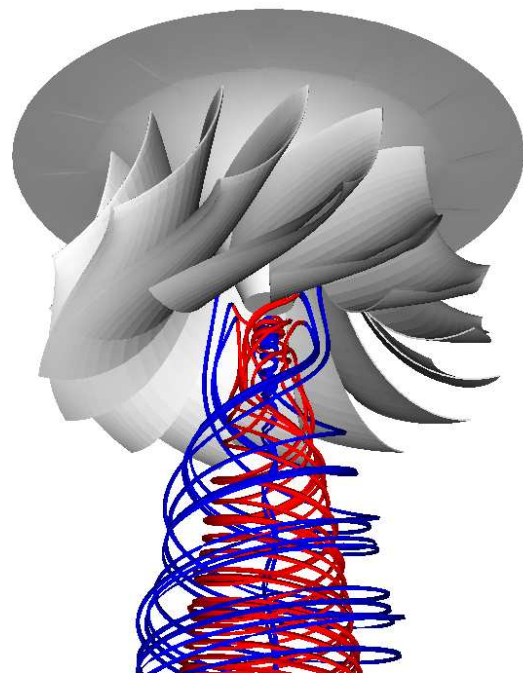
5.3 Static pressure iso-surfaces

During the measurements of the best efficiency operating point, it was visually observed that cavitation was developed at the leading edge suction side, close to the shroud. The runner blade static pressure measurements also revealed this low static pressure region. The computations do

not show such a distinct static pressure reduction when the surface static pressure is examined (in figures 4.10-4.14). However, an iso-surface of low static pressure shows that the computations qualitatively capture this feature. This is shown in figure 5.3(a) by the static pressure coefficient iso-surface $C_p = -0.25$ for the best efficiency operating point. Apart from a clear low pressure region at the leading edge suction side close to the shroud, there is an indication of low pressure close to the axis of rotation. This can be expected, since a vortex core is centered at the axis of rotation and the static pressure is reduced in vortex cores. The static pressure coefficient iso-surface behaviour is similar for all operating points except operating point 2. For operating point 2, the main static pressure coefficient reduction is at the rotational axis, beneath the hub (figure 5.3(b)). There is strong recirculation in this region for this operating condition. There is no distinct static pressure reduction at the leading edge of the suction side close to the shroud as for the other operating conditions. Still, there are some regions of low static pressure at the suction side very close to the surface. The levels of the iso-surfaces in figures 5.3(a) and 5.3(b) are not the same, since the iso-surfaces in figure 5.3(a) become too small for $C_p = -0.3$ and the iso-surfaces in figure 5.3(b) become too large for $C_p = -0.25$.

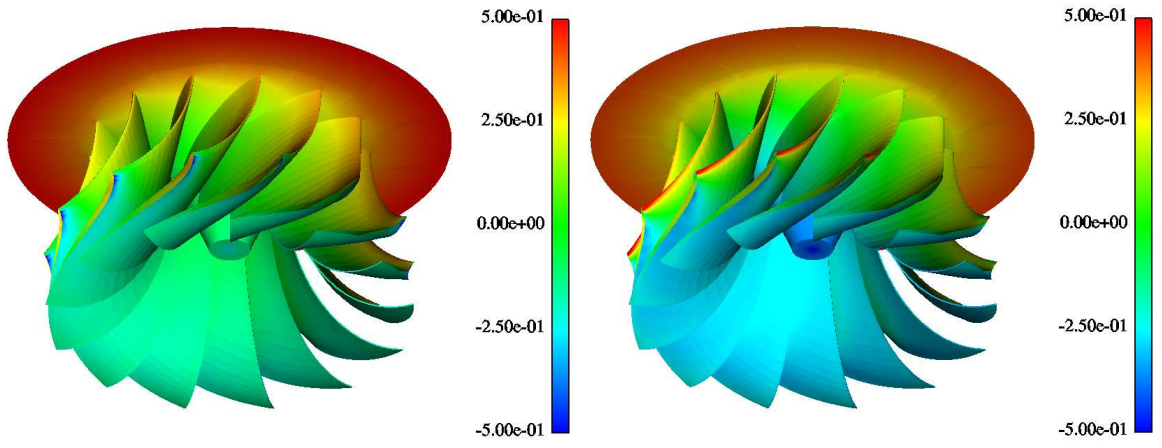


(a) Operating point 1.



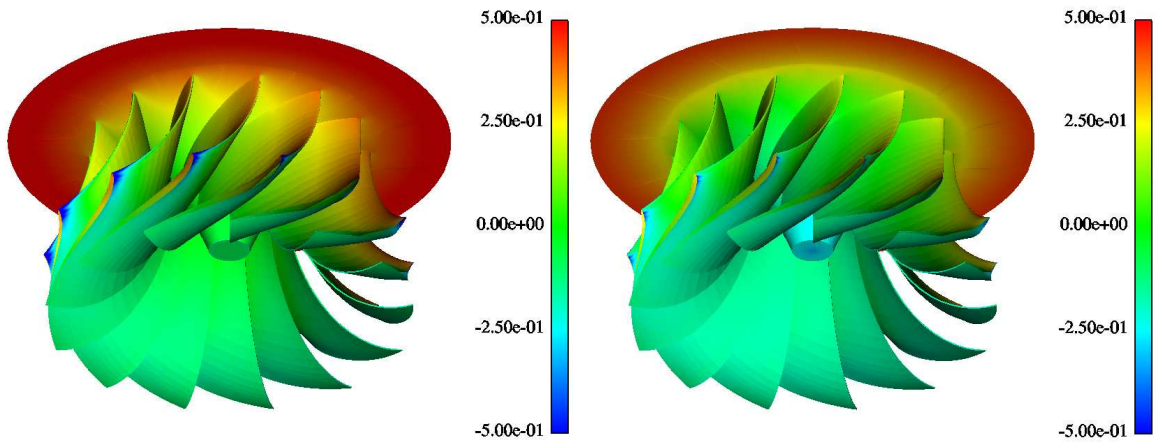
(b) Operating point 2.

Figure 5.1: A comparison of the flow beneath the hub for the best efficiency operating condition (Operating point 1) and for the worst (Operating point 2). The streamlines are colored blue when the flow is downwards and red when it is upwards.



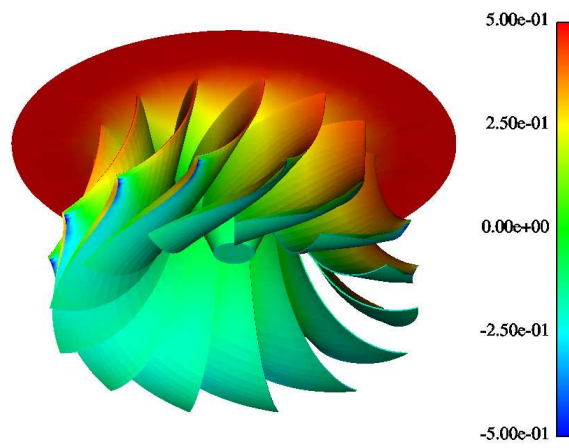
(a) Operating point 1.

(b) Operating point 2.



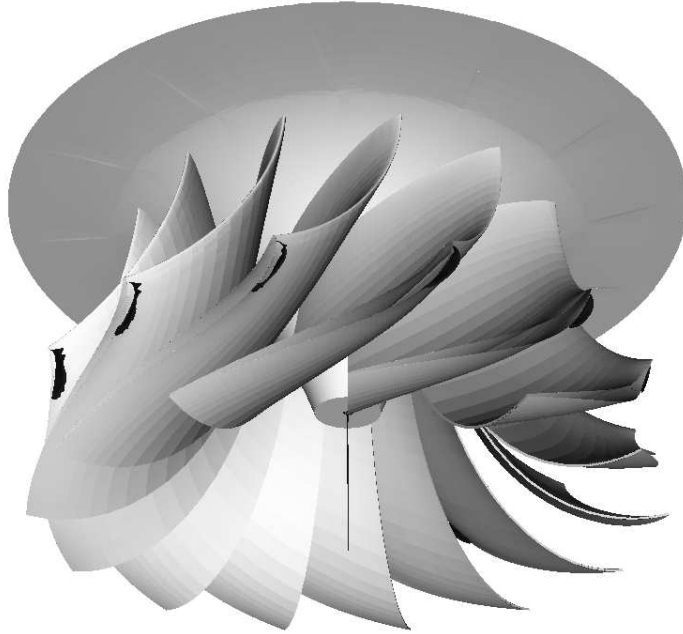
(c) Operating point 3.

(d) Operating point 4.

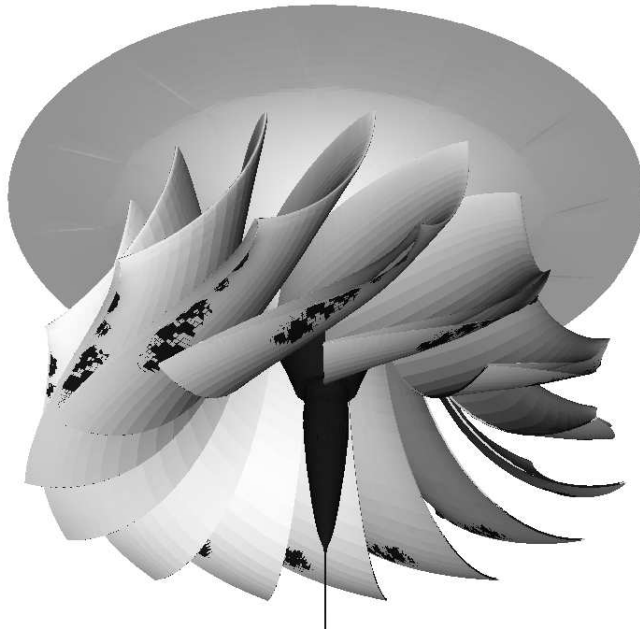


(e) Operating point 5.

Figure 5.2: Surface static pressure coefficient, C_p , distributions.



(a) Pressure coefficient iso-surface, $C_p = -0.25$ (colored dark), operating point 1.



(b) Pressure coefficient iso-surface, $C_p = -0.3$ (colored dark), operating point 2.

Figure 5.3: Pressure coefficient iso-surfaces.

6 Conclusion

Numerical computations have been made of the turbulent flow in the GAMM Francis runner at the best efficiency and four off-design operating conditions. Comparisons with measurements done at IMH-IMHEF-EPFL show that the CALC-PMB CFD code qualitatively captures most of the flow features. Some discrepancies in the comparisons arise particularly at low mass flow in regions where recirculation and unsteadiness dominate the flow. To predict these flow features, however, non-periodic transient computations must be made, which is beyond the scope of this work. To make these studies, it would also be necessary to make complementary measurements that study the recirculation regions and the transient effects in detail.

It is difficult to say anything about the quantitative results, since there were uncertainties in some of the measurements. It was especially difficult to experimentally determine the specific energy of the turbine, which was used for normalizing all the other quantities. Some details, such as a discrepancy between the measured velocity profile (which was argued to be quite axi-symmetric) and the volume flow and a discrepancy between the best efficiency and the corresponding torque, make the measurements somewhat less reliable. The fact that the experimental results had to be recovered from non-original files, where some of the information was lost and other information was not feasible, did not contribute to the reliability of the measurements. It would be desirable to have a more detailed and complete measurement database of a simpler application with more defined boundary conditions with which to validate CFD codes. Yet, this is the best measurement database of a hydraulic turbine that is publically available, since most detailed measurements are kept confidential by the companies that perform them.

The computational results in this work show great similarity with the computational results from the TASCflow CFD code, which produced the best results of the codes used for the computations in Gros *et al.* [7]. It was argued, however, that the N3S CFD code was better able to predict a low pressure peak on the suction side near the leading edge and close to the shroud, where cavitation development was observed during the experiments. In the runner blade static pressure distributions presented in this work, this low pressure peak is not clear. It can however readily be observed by using an iso-surface of low static pressure.

The simple and stable $k - \omega$ eddy viscosity turbulence model by Wilcox [18] is used in this work. This kind of turbulence model does not perform well in all the flow features in water turbines. However, experience shows that the turbulence model affects the flow less than discretization effects for this kind of complex geometries. The use of a low Reynolds number turbulence model such as this one makes it possible to resolve the turbulent boundary layers. This removes the log law assumption commonly used in industrial applications. It also makes possible tip clearance computations of Kaplan runners, which is being done using CALC-PMB in ongoing work.

The validation done in this work shows that the parallel multiblock CALC-PMB CFD code can be relied upon in predictions the turbulent flow in hydraulic machinery.

References

- [1] F. Avellan, P. Dupont, M. Farhad, B. Gindroz, P. Henry, M. Hussein, E. Parkinson, and O. Santal. Experimental flow study of the GAMM turbine model. In G. Sottas and I. L. Rhyming, editors, *3D-Computations of Incompressible Internal Flows - Proceedings of the GAMM Workshop at EPFL, September 1989, Lausanne - Notes on Numerical Fluid Mechanics*, pages 33–53. Vieweg, Braunschweig, 1993.
- [2] E. Blosch, W. Shyy, and R. Smith. The role of mass conservation in pressure-based algorithms. *Numer. Heat Transfer. Part B*, 24:415–429, 1993.
- [3] D. Cobut, Y.P. Marx, J.D. Reymond, M.L. Sawley, and L. Bellet. A numerical study of the flow in a Francis turbine runner at off-design operating conditions. In *Conference on Modeling, Testing & Monitoring for Hydro Powerplants - II, IMHEF Report T-96-14*, 1996.
- [4] L. Davidson. An introduction to turbulence models. Int.rep. 97/2, Thermo and Fluid Dynamics, Chalmers University of Technology, Gothenburg, 1997.
- [5] L. Davidson and B. Farhanieh. CALC-BFC: A Finite-Volume Code Employing Collocated Variable Arrangement and Cartesian Velocity Components for Computation of Fluid Flow and Heat Transfer in Complex Three-Dimensional Geometries. Rept. 92/4, Thermo and Fluid Dynamics, Chalmers University of Technology, Gothenburg, 1992.
- [6] J.P. Van Doormaal and G.D. Raithby. Enhancements of the SIMPLE method for predicting incompressible fluid flows. *Num. Heat Transfer*, 7:147–163, 1984.
- [7] L. Gros, J.L. Kueny, F. Avellan, and L. Bellet. Numerical flow analysis of the GAMM turbine at nominal and off-design operating conditions. In *Proceedings of the XIX IAHR Symposium, Hydraulic Machinery and Cavitation*, pages 121–128, 1998.
- [8] T. Kubota. Normalization of flow profile data measured at runner inlet. In G. Sottas and I. L. Rhyming, editors, *3D-Computations of Incompressible Internal Flows - Proceedings of the GAMM Workshop at EPFL, September 1989, Lausanne - Notes on Numerical Fluid Mechanics*, pages 55–62. Vieweg, Braunschweig, 1993.
- [9] P.K. Kundu. *Fluid Mechanics*. Academic Press, San Diego, California, 1990.
- [10] J. Larsson. Numerical simulation of turbulent flows for turbine blade heat transfer applications. Technical report, Dept. of Thermo and Fluid Dynamics, Chalmers University of Technology, Gothenburg, 1998.
- [11] H. Nilsson. A Numerical Investigation of the Turbulent Flow in a Kaplan Water Turbine Runner. Thesis for the degree of Licentiate of Engineering 99/5, Dept. of Thermo and Fluid Dynamics, Chalmers University of Technology, Gothenburg, 1999.
- [12] H. Nilsson, S. Dahlström, and L. Davidson. Parallel multiblock CFD computations applied to industrial cases. *To be published in the proceedings of ParCFD2000*, 2000.
- [13] H. Nilsson and L. Davidson. CALC-PVM: A parallel SIMPLEC multiblock solver for turbulent flow in complex domains. Int.rep. 98/12, Dept. of Thermo and Fluid Dynamics, Chalmers University of Technology, Gothenburg, 1998.
- [14] H. Nilsson and L. Davidson. A numerical comparison of four operating conditions in a Kaplan water turbine, focusing on tip clearance flow. In *Proceedings of the 20th IAHR Symposium, Hydraulic Machinery and Cavitation*, 2000.

- [15] E. Parkinson. Turbomachinery Workshop ERCOFTAC II, Test Case 8: Francis turbine, 1995.
- [16] S.V. Patankar. *Numerical Heat Transfer and Fluid Flow*. McGraw-Hill, New York, 1980.
- [17] G. Sottas and I. L. Ryhming, editors. *3D-Computations of Incompressible Internal Flows - Proceedings of the GAMM Workshop at EPFL, September 1989, Lausanne - Notes on Numerical Fluid Mechanics*. Vieweg, Braunschweig, 1993.
- [18] D.C. Wilcox. Reassessment of the scale-determining equation for advanced turbulence models. *AIAA J.*, 26(11):1299–1310, 1988.